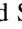












The Ionization and Dynamics of the Makani Galactic Wind

David S. N. Rupke¹ , Alison L. Coil² , Serena Perrotta² , Julie D. Davis³, Aleksandar M. Diamond-Stanic⁴, James E. Geach⁵, Ryan C. Hickox⁶ , John Moustakas⁷ , Grayson C. Petter⁶ , Gregory H. Rudnick⁸ , Paul H. Sell⁹ , Christy A. Tremonti³, and Kelly E. Whalen⁶ 

¹Department of Physics, Rhodes College, 2000 North Parkway, Memphis, TN 38112, USA; drupke@gmail.com

²Center for Astrophysics and Space Sciences, University of California, San Diego, La Jolla, CA 92093, USA

³Department of Astronomy, University of Wisconsin–Madison, Madison, WI 53706, USA

⁴Department of Physics and Astronomy, Bates College, Lewiston, ME 04240, USA

⁵Centre for Astrophysics Research, University of Hertfordshire, Hatfield, Hertfordshire AL10 9AB, UK

⁶Department of Physics and Astronomy, Dartmouth College, Hanover, NH 03755, USA

⁷Department of Physics and Astronomy, Siena College, Loudonville, NY 12211, USA

⁸Department of Physics and Astronomy, University of Kansas, Lawrence, KS 66045, USA

⁹Department of Astronomy, University of Florida, Gainesville, FL, 32611 USA

Received 2022 September 2; revised 2023 February 3; accepted 2023 February 17; published 2023 April 18

Abstract

The Makani galaxy hosts the poster child of a galactic wind on scales of the circumgalactic medium. It consists of a two-episode wind in which the slow, outer wind originated 400 Myr ago (Episode I; $R_I = 20 - 50$ kpc) and the fast, inner wind is 7 Myr old (Episode II; $R_{II} = 0 - 20$ kpc). While this wind contains ionized, neutral, and molecular gas, the physical state and mass of the most extended phase—the warm, ionized gas—are unknown. Here we present Keck optical spectra of the Makani outflow. These allow us to detect hydrogen lines out to $r = 30 - 40$ kpc and thus constrain the mass, momentum, and energy in the wind. Many collisionally excited lines are detected throughout the wind, and their line ratios are consistent with $200 - 400 \text{ km s}^{-1}$ shocks that power the ionized gas, with $v_{\text{shock}} = \sigma_{\text{wind}}$. Combining shock models, density-sensitive line ratios, and mass and velocity measurements, we estimate that the ionized mass and outflow rate in the Episode II wind could be as high as those of the molecular gas: $M_{II}^{\text{HII}} \sim M_{II}^{\text{H}_2} = (1 - 2) \times 10^9 M_{\odot}$ and $dM/dt_{II}^{\text{HII}} \sim dM/dt_{II}^{\text{H}_2} = 170 - 250 M_{\odot} \text{ yr}^{-1}$. The outer wind has slowed, so that $dM/dt_I^{\text{HII}} \sim 10 M_{\odot} \text{ yr}^{-1}$, but it contains more ionized gas, $M_I^{\text{HII}} = 5 \times 10^9 M_{\odot}$. The momentum and energy in the recent Episode II wind imply a momentum-driven flow (p “boost” ~ 7) driven by the hot ejecta and radiation pressure from the Eddington-limited, compact starburst. Much of the energy and momentum in the older Episode I wind may reside in a hotter phase, or lie further into the circumgalactic medium.

Unified Astronomy Thesaurus concepts: Galactic winds (572); Stellar feedback (1602); Starburst galaxies (1570); Circumgalactic medium (1879); Shocks (2086)

Supporting material: figure set

1. Introduction

The circumgalactic medium (CGM) of galaxies contains at least 80% of the baryonic mass within their dark matter halos (Shull et al. 2012; Werk et al. 2014; Tumlinson et al. 2017). The CGM is also home to $>50\%$ of the metals within a halo (Bordoloi et al. 2014; Peeples et al. 2014; Oppenheimer et al. 2016). The origin of this gas is likely diverse, but an important source is metal-enriched gas ejected from galaxies by galactic winds.

Catching galactic winds in the act of depositing gas in the CGM has proven challenging, as the observed sizes of these winds are typically comparable to the scales of the galaxies themselves (of order $\lesssim 10$ kpc). We reported in Rupke et al. (2019) a 100 kpc nebula surrounding the Makani galaxy at $z = 0.459$. The galaxy Makani (SDSS J211824.06+001729.4) is a massive ($M_{\odot} = 10^{11.1}$) star-forming galaxy with $r_e = 2.5$ kpc (Sell et al. 2014). The nebula, observed in [O II] $\lambda\lambda 3726, 3729$, is consistent with two galactic wind episodes over the past ~ 400 Myr, based on analysis of its morphology, kinematics, and stellar populations. Episode I was powered by a star formation

episode 400 Myr in the past and includes most of the outer 20–50 kpc of the wind. This wind has slow projected speeds $\sim 100 \text{ km s}^{-1}$ and line widths $\sigma = 200 \text{ km}^{-1}$, with a shape characteristic of a giant, bipolar outflow. The star formation timescale, projected ballistic flow speed, and radius of this flow are consistent: $\langle v \rangle_I \sim R_I/t_{*,I} = 50 \text{ kpc}/400 \text{ Myr} = 120 \text{ km s}^{-1}$. Episode II was powered by star formation a mere 7 Myr ago and consists of a fast wind with maximum speeds exceeding 2000 km s^{-1} , similar to the extended, high-velocity flow seen in other compact starbursts (Geach et al. 2014). Most of the Episode II wind is within 20 kpc of the host galaxy, though there is a faint southern extension to 40 kpc. As with Episode I, the approximate timescale, speed, and size line up: $\langle v \rangle_{II} \sim R_{II}/t_{*,II} = 10 \text{ kpc}/7 \text{ Myr} = 1400 \text{ km s}^{-1}$. The overall size of the Episode I+II nebula relative to the parent galaxy ($r_{\text{wind}}/r_{e,*} \gtrsim 20$) is direct evidence that the wind has moved into the galaxy’s CGM.

The KCWI observations covered only blue wavelengths and emission lines from [O II], Mg II $\lambda\lambda 2796, 2803$, and [Ne V] $\lambda\lambda 3345, 3426$. They thus leave unanswered two important questions regarding the ionized gas in the Makani wind. First, the ionized mass in the wind cannot be determined without recombination-line measurements. Second, the ionization state of the wind is unknown. The former is critical for constraining the

impact of the wind on its host and surroundings; the second is important for understanding its interaction with the CGM. An understanding of how the nebula is powered may also inform how it is driven.

The spatially resolved molecular component of the Episode II wind in Makani is outflowing with similar velocities to the ionized gas at a rate of $245 M_{\odot} \text{ yr}^{-1}$ (Rupke et al. 2019). This suggests a rapid exhaustion of star formation fuel, at a level comparable to the star formation rate (SFR) of several hundred $M_{\odot} \text{ yr}^{-1}$ (Petter et al. 2020). The ionized mass of either wind episode is unknown, however, and since no other gas phases have yet been observed in the extended Episode I wind, we do not know its outflow rate. In its time-resolved structure, Makani presents a unique opportunity to constrain the evolution of outflow rates with time.

Due to its compact size, most of the host galaxy itself is unresolved in ground-based observations. Based on Keck/NIRSPEC, MMT long-slit, and Sloan Digital Sky Survey (SDSS) data, we know that the unresolved host emission—which includes a narrow, near-systemic component and a broad, blueshifted component that dominates the flux—lies in the active galactic nucleus (AGN) area of excitation diagrams (Rupke et al. 2019; Perrotta et al. 2021). The outflowing component in the galaxy also shows weak [Ne V] $\lambda\lambda 3345, 3426$ emission (Rupke et al. 2019). Normally these would be indicative of an AGN, but Makani shows no other evidence of an AGN (Sell et al. 2014; Rupke et al. 2019). We have tentatively interpreted these as evidence of high-velocity shocks as the Episode II wind propagates through the gas in the center of the galaxy. However, it is also possible that the ionization of the Makani host galaxy and that of its parent sample (Tremonti et al. 2007) reflect leakage of Lyman continuum (LyC) photons (Perrotta et al. 2021). Further constraining its ionization may distinguish between these scenarios.

To address these questions, here we present Keck/ESI long-slit spectra of Makani in the optical. In Section 2, we present the observations, data reduction, and data analysis. We describe the results in Section 3, and we discuss them in light of shock and outflow models in Section 4. We summarize in Section 5.

2. Observations and Data Processing

We observed Makani on 2020 September 12 UT with the Echelle Spectrograph and Imager (ESI; Sheinis et al. 2002) on Keck II. We chose the $1''.0$ slit in echelle mode, which yields moderate velocity resolution ($R = 4000$). The broad, simultaneous wavelength coverage allows us to observe many rest-frame optical strong lines ([O II] through [S II] $\lambda\lambda 6716, 6731$), while the $20''$ slit length is well matched to the extent of the $17''$ nebula.

Conditions were photometric, with seeing $\lesssim 0''.8$. We took 3×30 -minute exposures centered on the galaxy with PA = 45° east of north and 4×30 -minute exposures centered on a point offset $3''.3$ west at PA = 0° (Figure 1). These slit positions were designed to probe the highest surface brightness regions of the nebula outside of the nucleus while catching significant areas of low surface brightness features. To calibrate, we took bias, arc lamp, dome flat, twilight flat, and pinhole flat observations. We dithered $\pm 1''$ along the slit between exposures. We observed the flux standard BD +28 4211 for photometric and telluric corrections. Air masses were 1.06–1.07 for the flux standard and PA = 45° slit and 1.1–1.4 for the PA = 0° slit.

We reduce the data using the ESIRedux package (Prochaska et al. 2003) in XIDL. We use all calibrations except the twilight

flats. We additionally telluric-correct the spectra using the flux standard after normalizing it by an 82,000 K blackbody. The final spectra are in vacuum wavelengths.

Along each slit, we extract five apertures (Figure 1 and Table 1, labeled in order of increasing projected galactocentric radius). The lengths of the inner apertures are $2 \times \text{FWHM}_{\text{seeing}}$ (10 pixels, or $1''.54$), and those of the outer apertures are $4 \times \text{FWHM}_{\text{seeing}}$ (20 pixels, or $3''.08$). We coadd the two overlapping apertures (ap7). We searched for emission in apertures outside the previously detected nebula but found none that surpassed the detection threshold.

We extract a $3'' \times 1''$ rectangular aperture centered on the galaxy to compare to the existing $3''$ -diameter SDSS spectrum. The SDSS spectrum is 26% higher in flux over 6500–9000 Å, but the difference rises smoothly with decreasing wavelength to 80% at 4000 Å. This flux difference is also observed in a $3''$ circular extraction from the KCWI data cube. We apply this upward correction to each extracted spectrum. The effect on flux ratios is minimal but may be 5% for [O II]/H α , as the total upward correction at [O II] is 33%.

We fit the spectra using IFSFIT (Rupke 2014). We fit the continuum with pPXF (Cappellari 2012, 2017) and the same C3K solar-metallicity stellar models (Conroy et al., in preparation) used in Rupke et al. (2019). We use the best-fit stellar model to the host spectrum (ap1) as a template for the two $r \sim 10$ kpc apertures (ap2 and ap3), which also contain some stellar emission. In these fits, we allow for nonzero stellar attenuation and include an order-4 additive polynomial to account for uncertainties in data reduction (flux calibration, scattered light, etc.). The only aperture with a nonzero best-fit stellar attenuation is ap1, for which $E(B - V)_* = 0.3$. There are no visible stellar continua in other apertures, though very low levels of continuum flux may indicate imperfect sky subtraction in some cases. To remove this residual signal, we fit an order-10 polynomial continuum.

After subtracting the best-fit continuum model, we fit two velocity components—one narrow and approximately systemic, the other broad and blueshifted—to the emission lines in ap1, ap2, and ap3, and one component otherwise (Figure 2). (Hereafter we refer to the narrow, near-systemic component of ap1 as ap1.1 and the broad, blueshifted component of ap1 as ap1.2.) These components are robustly detected in the host galaxy, and we treat them separately in some parts of the analysis. While multiple components (including the same broad line seen in ap1) are clearly required in ap2 and ap3, the lower signal-to-noise ratio (S/N) in some lines means that these components are not significantly detected in every line. For instance, [S II] suffers from lower throughput and sky-line contamination. Thus, in our analysis we treat only the total flux for ap2 and ap3. For these apertures, we also fix the [O II] $\lambda 3729/\lambda 3726$ flux ratios to match that of ap1.

For the most part, the velocities and line widths of all emission lines are tied together. However, we find that the fit to [O I] in apertures ap1, ap4, and ap5 is improved if we fit its velocity and line width separately. (In other apertures, the line is too faint to fit separately.) The most significant difference is that in ap1 the broad component in [O I] is redshifted compared to the broad component in other lines by $\Delta v = 350 \text{ km s}^{-1}$ and narrower by $\Delta \sigma = 200 \text{ km s}^{-1}$ (40% smaller). In the narrow component of ap1 and in ap4 and ap5, [O I] is only slightly redshifted ($\lesssim 50 \text{ km s}^{-1}$) and the line width difference is small ($\lesssim 30 \text{ km s}^{-1}$).

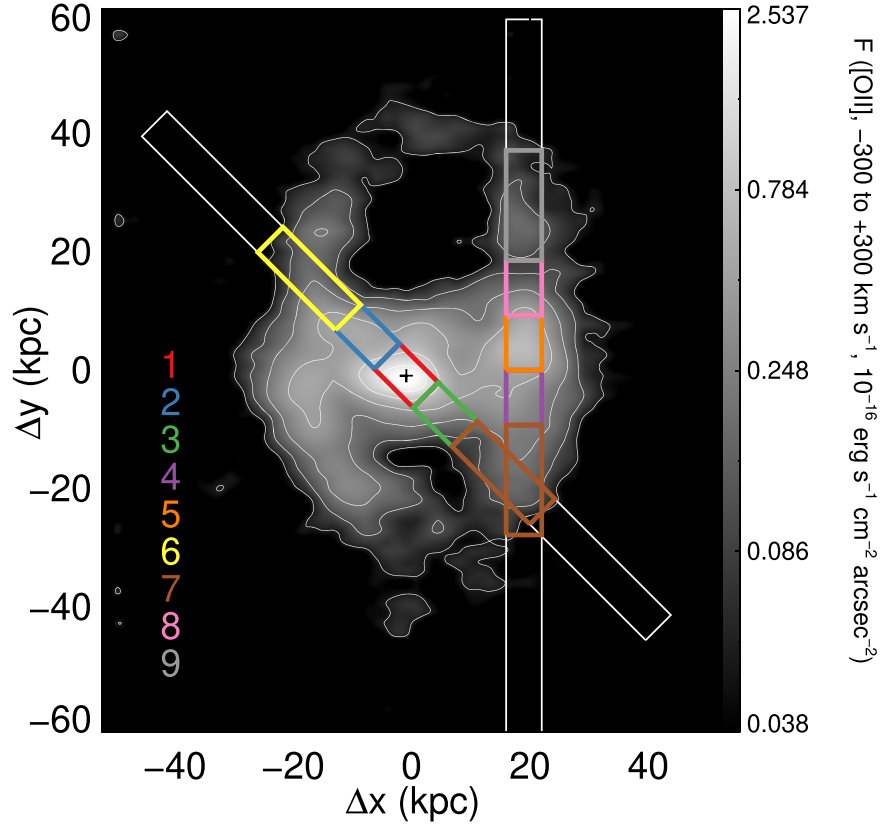


Figure 1. The Makani [O II] nebula as observed by KCWI (Rupke et al. 2019), with ESI long slits overlaid. The peak [O II] KCWI spaxel is labeled with a plus sign. The extracted apertures are shown as colored boxes. North is up and east is to the left. The grayscale is [O II] flux integrated from -300 to $+300$ km s^{-1} , in units of $10^{-16} \text{ erg s}^{-1} \text{ cm}^{-2} \text{ arcsec}^{-2}$.

Table 1
Apertures

Label	Size	Radius (kpc)	$f([\text{O II}])/10^{-16}$ ($\text{erg s}^{-1} \text{ cm}^{-2}$)
(1)	(2)	(3)	(4)
ap1	$1'' \times 1''54$	$0.0^{5.5}$	7.74 ± 0.26
ap2	$1'' \times 1''54$	$9.3_{3.8}^{5.0}$	2.30 ± 0.08
ap3	$1'' \times 1''54$	$9.3_{3.8}^{5.0}$	1.50 ± 0.11
ap4	$1'' \times 1''54$	$20.2_{3.3}^{4.1}$	0.75 ± 0.03
ap5	$1'' \times 1''54$	$20.6_{3.8}^{4.4}$	1.41 ± 0.03
ap6	$1'' \times 3''08$	$23.2_{9.0}^{9.4}$	0.94 ± 0.06
ap7	$1'' \times 3''08$	$23.2_{9.0}^{9.4}$	0.39 ± 0.05
ap8	$1'' \times 1''54$	$24.8_{5.1}^{5.3}$	0.45 ± 0.02
ap9	$1'' \times 3''08$	$35.0_{9.2}^{9.4}$	0.19 ± 0.02

Note. Column (2): aperture extraction size. Column (3): radius of the aperture center, plus or minus the full range of radii represented by the boundaries of the aperture. Column (4): observed [O II] $\lambda\lambda 3726, 3729$ flux in the aperture, with 1σ errors.

In several apertures (ap2, ap7, and ap9) we first fit [O II] only and use the resulting line centers and line widths as fixed priors for the other lines. As this line is the brightest and has the highest S/N, this serves to improve the fit for faint lines ([O I]), lines impacted by sky contamination (in the red), and lines with some degeneracy due to blending ($\text{H}\alpha$ and [N II]).

In ap9, $\text{H}\alpha$ is only marginally detected, as it is impacted by sky lines. For this aperture, we instead estimate $\text{H}\alpha$ from $\text{H}\beta$ assuming no extinction and the case B ratio of 2.86.

There is residual interstellar Na I D absorption and emission in two apertures, ap1 and ap2. We fit these features also using IFSFIT (Figure 3), and we report the results in Section 3.2.

3. Results

The high throughput and long wavelength coverage of ESI allow us to detect numerous strong emission lines across the nebula. The ap1 spectrum also includes weak emission lines such as [Ne V] $\lambda 3426$, [O III] $\lambda 4363$, and [N II] $\lambda 5755$. We report observed and extinction-corrected line fluxes of all emission lines detected at $>2\sigma$ in Table 2, as well as $\text{H}\alpha$ fluxes and luminosities. Observed fluxes have been corrected for a Galactic extinction of $E(B - V) = 0.0684$ (Schlafly & Finkbeiner 2011).

The ESI spectra cover the full range of Balmer lines. In Figure 4, we show observed [O II] and $\text{H}\alpha$ surface brightnesses as a function of radius. The ratio steadily rises from about 1/3 in the center, to unity at 20 kpc, and finally to a maximum of 2 at $r = 30\text{--}40$ kpc. This increase in observed [O II]/ $\text{H}\alpha$ is due to a combination of decreasing extinction and increasing collisional excitation with increasing radius. We compute $E(B - V)$ from $\text{H}\alpha/\text{H}\beta$ for case B conditions using the Cardelli et al. (1989) extinction curve and $R_V = 3.1$. $E(B - V)$ decreases with increasing radius from a peak of 1.0 at $r = 10$ kpc to 0 at $r > 25$ kpc (Figure 4). The intrinsic [O II]/ $\text{H}\alpha$ flux ratio is near unity in ap1 and ap3, rising to a value of 2–5 in larger-radius apertures.

By combining the ESI $\text{H}\alpha$ and KCWI [O II] measurements, we can estimate the spatially resolved and integrated $\text{H}\alpha$ luminosity. We do so by bootstrapping from the ESI

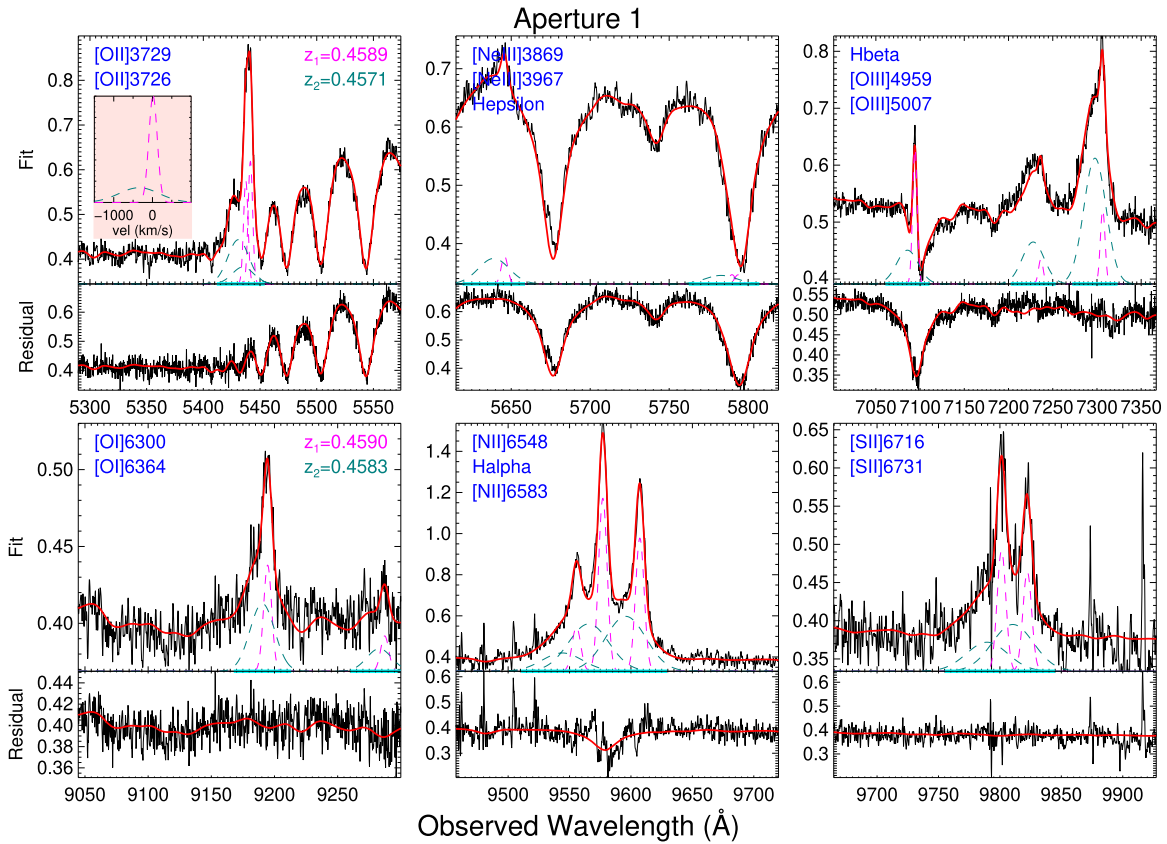


Figure 2. Observed spectrum of each aperture and model fits near strong emission lines. In each panel, the lines plotted are in the upper left corner. The black line is the data, in units of 10^{-16} erg s^{-1} cm^{-2} \AA^{-1} ; the red line is the total model fit (lines+continuum); and dashed lines are the emission-line model. Different velocity components are shown as different colors. The best-fit redshift of each component is shown in the [O II] panel, as is an inset showing the velocity profile of [O II] λ 3729. Because the velocity of [O I] is allowed to vary separately in some apertures, its best-fit redshifts are shown in the corresponding panel. The data are smoothed with a 3-pixel boxcar. The data and model residuals after subtraction of the emission-line model (black and red lines) and the 1σ error in the data (teal line) are shown in the bottom third of each panel.

(The complete figure set (9 images) is available.)

measurements to estimate how the ratio ($[\text{O II}]$, observed)/($H\alpha$, intrinsic) changes with radius. We fit a linear relationship between 0 and 35 kpc (Figure 4) with an rms of 0.3 dex. We then apply this relationship to the Voronoi-binned KCWI data to infer the spatially resolved $H\alpha$ flux. The resulting total $H\alpha$ luminosity is $L_{H\alpha}^{\text{tot}} = (9.4_{-3.0}^{+6.0}) \times 10^{42}$ erg s^{-1} , where we calculate the error by applying the rms dispersion at $r > 5.5$ kpc (the edge of ap1). (Using instead a parabolic fit increases the luminosity by 15%, but it does not change the rms and results in line ratios at the edge of the wind— $r \sim 50$ kpc—that appear unphysical.)

We calculate the electron density using the flux ratios $[\text{O II}] \lambda 3729 / \lambda 3726$ and $[\text{S II}] \lambda 6716 / \lambda 6731$, which are allowed to freely vary between physical limits (Sanders et al. 2016). Both lines are observed throughout the nebula, though [S II] is not detected in all apertures. The [O II] doublet is one of the brightest lines in the rest-frame optical spectrum of the nebula and is unaffected by sky lines. However, the lines are separated by only 3 \AA , leading to covariance among fit parameters. Overlap of multiple velocity components adds further degeneracy. While the [S II] lines are better separated in wavelength (15 \AA), they are impacted by sky lines and fall in a lower-sensitivity part of the data. Thus, we report density estimates only in ap1, ap4, and ap5; the significance of the individual line detections of the [S II] doublet, and thus our ability to reliably

decompose them, is too low in other apertures, even if the total doublet is detected.

In ap1.1, densities are $\log(n_e/\text{cm}^{-3}) = 2.3_{-0.6}^{+0.3}$ and $2.3_{-0.3}^{+0.2}$ from [S II] and [O II], respectively. The ap1.2 (higher σ , blueshifted) densities are $3.4_{-0.4}^{+0.6}$ and $>4.0_{-0.9}$. For ap4 and ap5, $\log(n_e/\text{cm}^{-3}) < 1$ from both line ratios, in both apertures. The upper error bar is rather large (1.5–2.3 dex) on the ap4–ap5 measurements, however, due to the decreasing sensitivity of the line ratios to densities below $\sim 50 \text{ cm}^{-3}$.

3.1. Excitation of the Wind

The detection of multiple emission lines throughout the Makani nebula allows us to constrain the spatially resolved excitation of the wind using standard line ratios (Figure 5; Baldwin et al. 1981; Veilleux & Osterbrock 1987; Cid Fernandes et al. 2010).

Beginning with the nucleus, ap1, we find that the broad component dominates its line flux and is securely in the AGN region of these diagrams. This is consistent with previous results (Perrotta et al. 2021). We extend this conclusion to the [O I]/ $H\alpha$ versus [O III]/ $H\beta$ and [O I]/ $H\alpha$ versus [O III]/[O II] diagrams, based on our detection of [O I]. Perrotta et al. (2021) interpreted these line ratios as ionization from fast shocks; we discuss this in detail in Section 4. Makani lacks evidence for an AGN in the rest-frame UV, X-ray, radio, or infrared (Diamond-

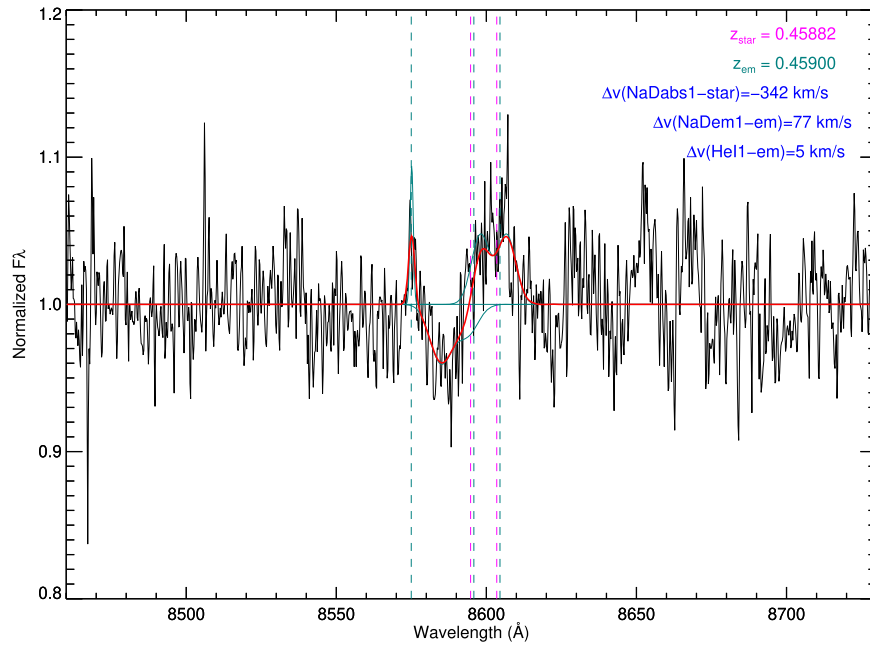


Figure 3. Fit to He I $\lambda 5876$ emission and Na I D $\lambda\lambda 5890, 5896$ absorption and emission in the central spectrum, ap1. Vertical dashed lines show the expected wavelengths based on our fit to the stellar continuum (magenta) and [O I] emission lines (teal) in ap1. Velocities with respect to these reference redshifts (z_{star} for Na I D absorption and z_{em} otherwise) are shown in the upper right corner.

Stanic et al. 2012; Sell et al. 2014; Petter et al. 2020; Whalen et al. 2022). The rest-frame optical–UV continuum of Makani shows no indication of nonstellar emission, and a stellar population fit to the spectral energy distribution is perfectly consistent with the data (Rupke et al. 2019). Though [Ne V] emission is present, its luminosity is low compared to AGNs (Rupke et al. 2019). We thus discount AGN photoionization as the origin of these line ratios.

The narrow component of ap1 is instead likely ionized by stars, with some possible contribution from shocks based on its location in the composite region of the [N II]/ $H\alpha$ versus [O III]/ $H\beta$ diagram.

The two apertures with $r \sim 10$ kpc (ap2 and ap3) combine information from two velocity components, one broad and one narrow. Ap2 has line ratios similar to those from total fluxes in ap1, with higher low-ionization line ratios ([O I]/ $H\alpha$) and lower ionization parameter [O III]/[O II]. Apertures ap3, ap4, and ap5 have similar [O I]/ $H\alpha$ and [O III]/[O II] to ap2, but with lower high-ionization line ratios ([O III]/ $H\beta$), larger [S II]/ $H\alpha$, and slightly smaller [N II]/ $H\alpha$. Two other apertures with significant detections across several lines (ap6 and ap8) lie in roughly the same locations as the other apertures, but these apertures have low S/N in the weakest lines, so their positioning is more uncertain. The lines other than [O II] and $H\alpha$ in ap7 and ap9 are not strong enough to accurately place them in these diagrams, though ap9 does appear in several with large error bars.

Taken as a whole, the apertures other than ap1 lie largely in the composite region of the [N II]/ $H\alpha$ diagram and in the low-ionization nuclear emission-line region (LINER) area in the other three diagrams. An exception is aperture ap2, which lies in between the properties of ap1 and ap3. This aperture is in the direction of the most highly blueshifted molecular and ionized gas (Rupke et al. 2019). It must therefore include more flux from this higher-ionization wind component (mixed in with a

lower-ionization component) than ap3, which is at the same radius as ap2.

We detect the weak emission lines [O III] $\lambda 4363$ and [N II] $\lambda 5755$ in ap1 and [O III] $\lambda 4363$ in ap2. The [O III] $\lambda 4363/\lambda 5007$ line flux ratios in ap1 and ap1.2 are -1.1 dex. Ratios this high are observed in LINERs, implying high temperatures ($T \gtrsim 2 \times 10^4$ K; Nagao et al. 2001; Molina et al. 2018). Similarly, the ratio [N II] $\lambda 5755/\lambda 6548$ is in the range -1.3 to -1.4 , also consistent with $T \sim 2 \times 10^4$ K.

3.2. Neutral Wind Properties

Makani may be the highest-redshift system in which interstellar Na I D absorption and/or emission has been seen in a galactic wind. Resonant Na I D absorption is detected in the host galaxy (ap1) with a low equivalent width (rest-frame W_{eq} of $0.37^{+0.07}_{-0.05}$ Å), but blueshifted by -342 km s^{-1} (Figure 3). The outflow was not previously detected in resonant absorption in Mg II $\lambda\lambda 2796, 2803$ or Mg I transitions in the near-UV (Rupke et al. 2019). However, there is residual, weak Fe II $\lambda 2585$ absorption (Rupke et al. 2019; Perrotta et al. 2021).

Previously, redshifted resonant emission in Mg II, Mg I, and Fe II* was detected in Makani (Rupke et al. 2019). The Mg II is spatially resolved into an $r \sim 20$ kpc nebula. We now detect spatially extended Na I D emission in ap1 and ap2, with fluxes and rest-frame equivalent widths of $(3.2 \pm 0.2) \times 10^{-17}$ erg $\text{s}^{-1} \text{cm}^{-2}$ and $W_{\text{eq}} = -0.49 \pm 0.05$ Å in ap1 and $(2.0 \pm 0.2) \times 10^{-17}$ erg $\text{s}^{-1} \text{cm}^{-2}$ and $W_{\text{eq}} = -4.4 \pm 0.5$ Å in ap2.

Several lines of evidence suggest that resonant absorption in ap1 is filling in the emission, reducing the observed $|W_{\text{eq}}|$ and increasing $|v - v_{\text{sys}}|$ of both absorption and emission. First, a fit to Fe II $\lambda 2585$ gives a velocity at maximum depth of -100 km s^{-1} and a covering factor of 0.12, assuming that it is optically thick. Thus, $v_{\text{NaI}} - v_{\text{FeII}} \sim -200$ km s^{-1} . Furthermore, if the Na I D and Fe II absorption lines are

Table 2
Fluxes and Luminosities

Line (1)	ap1.1 ^a (2)	ap1.2 ^a (3)	ap1 (4)	ap2 (5)	ap3 (6)	ap4 (7)	ap5 (8)	ap6 (9)	ap7 (10)	ap8 (11)	ap9 (12)
[Ne V] λ 3426	...	-1.43 ± 0.19	-1.66 ± 0.20
[O II] λ 3726	-0.74 ± 0.03	-0.55 ± 0.02	-0.63 ± 0.02	-0.35 ± 0.03	-0.33 ± 0.05	-0.30 ± 0.04	-0.31 ± 0.02	-0.08 ± 0.07	-0.27 ± 0.06	-0.01 ± 0.06	-0.05 ± 0.09
[O II] λ 3729	-0.67 ± 0.04	-0.97 ± 0.05	-0.81 ± 0.03	-0.45 ± 0.03	-0.57 ± 0.07	-0.14 ± 0.04	-0.14 ± 0.02	0.08 ± 0.07	-0.42 ± 0.13	0.15 ± 0.06	0.11 ± 0.07
[O II] λ 3726 +[O II] λ 3729	-0.41 ± 0.03	-0.41 ± 0.02	-0.41 ± 0.02	-0.09 ± 0.03	-0.13 ± 0.05	0.09 ± 0.03	0.09 ± 0.02	0.31 ± 0.07	-0.04 ± 0.07	0.38 ± 0.05	0.34 ± 0.06
[Ne III] λ 3869	-1.42 ± 0.08	-0.89 ± 0.04	-1.05 ± 0.03	-0.94 ± 0.09	-1.12 ± 0.07	-0.58 ± 0.13	-0.88 ± 0.11	-0.77 ± 0.15	...
[O III] λ 4363	-1.86 ± 0.20	-1.37 ± 0.11	-1.52 ± 0.09	-1.05 ± 0.12
H β	-0.65 ± 0.01	-0.69 ± 0.02	-0.67 ± 0.01	-0.87 ± 0.06	-0.58 ± 0.06	-0.66 ± 0.05	-0.64 ± 0.03	-0.68 ± 0.13	-0.74 ± 0.11	-0.41 ± 0.07	-0.46 ± 0.22
[O III] λ 5007	-0.90 ± 0.03	-0.11 ± 0.02	-0.31 ± 0.01	-0.48 ± 0.04	-0.61 ± 0.06	-0.67 ± 0.07	-0.74 ± 0.04	-0.44 ± 0.11	...	-0.60 ± 0.11	-0.30 ± 0.21
[N I] λ 5198	-1.11 ± 0.07	...	-1.39 ± 0.08	-1.61 ± 0.09	-1.40 ± 0.11	-1.43 ± 0.11
+ [N I] λ 5200
[N II] λ 5755	-1.66 ± 0.11	-1.33 ± 0.09	-1.44 ± 0.07
[O I] λ 6300	-1.12 ± 0.08	-0.94 ± 0.09	-1.01 ± 0.06	-0.73 ± 0.05	-0.70 ± 0.07	-0.68 ± 0.08	-0.69 ± 0.04	-0.57 ± 0.09	-0.32 ± 0.15
[N II] λ 6583	-0.11 ± 0.02	0.07 ± 0.03	-0.00 ± 0.02	-0.20 ± 0.06	-0.31 ± 0.10	-0.46 ± 0.08	-0.48 ± 0.04	-0.20 ± 0.14	-0.60 ± 0.14	...	-0.06 ± 0.07
[S II] λ 6716	-0.72 ± 0.03	-0.77 ± 0.06	-0.75 ± 0.03	-0.54 ± 0.06	-0.24 ± 0.05	-0.17 ± 0.05	-0.34 ± 0.03	...	0.04 ± 0.04	-0.90 ± 0.15	...
[S II] λ 6731	-0.80 ± 0.05	-0.57 ± 0.11	-0.65 ± 0.08	-0.61 ± 0.10	-0.41 ± 0.06	-0.33 ± 0.06	-0.50 ± 0.04	-0.73 ± 0.14	-0.12 ± 0.05	-0.55 ± 0.08	...
[S II] λ 6716	-0.46 ± 0.03	-0.36 ± 0.07	-0.40 ± 0.05	-0.28 ± 0.06	-0.02 ± 0.05	0.06 ± 0.04	-0.11 ± 0.02	-0.57 ± 0.14	0.27 ± 0.04	-0.39 ± 0.08	...
+ [S II] λ 6731
$\log(F_{\text{H}\alpha})$	-15.063 ± 0.009	-14.952 ± 0.014	-14.703 ± 0.009	-15.55 ± 0.02	-15.69 ± 0.04	-16.21 ± 0.03	-15.94 ± 0.01	-16.34 ± 0.06	-16.37 ± 0.03	-16.72 ± 0.05	-17.06 ± 0.05
$E(B-V)$	0.454 ± 0.035	0.546 ± 0.056	0.505 ± 0.034	0.97 ± 0.14	0.30 ± 0.14	0.48 ± 0.12	0.42 ± 0.06	0.51 ± 0.30	0.67 ± 0.26	0.00 ± 0.17	0.00 ± 0.51
[NeV] λ 3426	...	-0.89 ± 0.20	-1.17 ± 0.21
[O II] λ 3726	-0.34 ± 0.04	-0.06 ± 0.06	-0.17 ± 0.04	0.52 ± 0.14	-0.06 ± 0.14	0.13 ± 0.12	0.07 ± 0.06	0.38 ± 0.29	0.33 ± 0.25	-0.01 ± 0.17	-0.05 ± 0.48
[O II] λ 3729	-0.27 ± 0.05	-0.48 ± 0.07	-0.36 ± 0.04	0.42 ± 0.14	-0.31 ± 0.15	0.29 ± 0.12	0.23 ± 0.06	0.54 ± 0.29	0.18 ± 0.27	0.15 ± 0.17	0.11 ± 0.48
[O II] λ 3726 +[O II] λ 3729	0.00 ± 0.04	0.08 ± 0.06	0.04 ± 0.04	0.77 ± 0.14	0.14 ± 0.14	0.52 ± 0.12	0.46 ± 0.06	0.77 ± 0.29	0.56 ± 0.25	0.38 ± 0.17	0.34 ± 0.48
[Ne III] λ 3869	-1.03 ± 0.08	-0.43 ± 0.07	-0.62 ± 0.05	-0.12 ± 0.16	-0.77 ± 0.09	-0.14 ± 0.31	-0.31 ± 0.26	-0.77 ± 0.21	...
[O III] λ 4363	-1.57 ± 0.20	-1.02 ± 0.12	-1.20 ± 0.10	-0.43 ± 0.17
H β	-0.46 ± 0.03	-0.46 ± 0.05	-0.46 ± 0.03	-0.46 ± 0.12	-0.46 ± 0.12	-0.46 ± 0.11	-0.46 ± 0.05	-0.46 ± 0.26	-0.46 ± 0.22	-0.41 ± 0.15	-0.46 ± 0.44
[O III] λ 5007	-0.73 ± 0.04	0.09 ± 0.04	-0.12 ± 0.03	-0.12 ± 0.11	-0.49 ± 0.12	-0.49 ± 0.11	-0.58 ± 0.06	-0.25 ± 0.25	...	-0.60 ± 0.17	-0.30 ± 0.43
[N I] λ 5198	-0.97 ± 0.07	...	-1.23 ± 0.09	-1.31 ± 0.13	-1.30 ± 0.15	-1.28 ± 0.14
+ [N I] λ 5200
[N II] λ 5755	-1.58 ± 0.11	-1.24 ± 0.10	-1.36 ± 0.07
[O I] λ 6300	-1.10 ± 0.08	-0.91 ± 0.09	-0.99 ± 0.07	-0.68 ± 0.10	-0.68 ± 0.11	-0.65 ± 0.11	-0.67 ± 0.05	-0.57 ± 0.14	-0.32 ± 0.36
[N II] λ 6583	-0.11 ± 0.03	0.06 ± 0.04	-0.01 ± 0.03	-0.20 ± 0.11	-0.31 ± 0.13	-0.46 ± 0.11	-0.48 ± 0.05	-0.20 ± 0.23	-0.60 ± 0.21	...	-0.06 ± 0.32
[S II] λ 6716	-0.73 ± 0.04	-0.79 ± 0.07	-0.76 ± 0.04	-0.57 ± 0.11	-0.25 ± 0.10	-0.19 ± 0.09	-0.35 ± 0.05	...	0.02 ± 0.16	-0.90 ± 0.18	...
[S II] λ 6731	-0.82 ± 0.06	-0.58 ± 0.11	-0.67 ± 0.08	-0.64 ± 0.13	-0.41 ± 0.10	-0.35 ± 0.10	-0.52 ± 0.05	-0.75 ± 0.23	-0.14 ± 0.17	-0.55 ± 0.13	...
[S II] λ 6716	-0.47 ± 0.04	-0.37 ± 0.08	-0.41 ± 0.05	-0.31 ± 0.10	-0.03 ± 0.10	0.04 ± 0.09	-0.13 ± 0.04	-0.59 ± 0.23	0.25 ± 0.16	-0.39 ± 0.13	...
+ [S II] λ 6731
$\log(L_{\text{H}\alpha})$	$42.32_{-0.02}^{+0.02}$	$42.52_{-0.03}^{+0.03}$	$42.73_{-0.02}^{+0.02}$	$42.36_{-0.07}^{+0.06}$	$41.53_{-0.08}^{+0.07}$	$41.20_{-0.07}^{+0.06}$	$41.41_{-0.03}^{+0.03}$	$41.10_{-0.18}^{+0.13}$	$41.22_{-0.14}^{+0.10}$	$40.20_{-0.10}^{+0.08}$	$39.86_{-0.32}^{+0.18}$

Note. Column (1): emission line. Columns (2)–(12), top half: \log of the observed line flux, normalized to H α . Fluxes have been corrected for Galactic extinction. Following are the \log of H α fluxes in $\text{erg s}^{-1} \text{cm}^{-2}$. Errors are 1σ in the \log . Middle: color excess, computed from H α /H β for case B conditions using the Cardelli et al. (1989) extinction curve and $R_V = 3.1$. Bottom half: \log of the extinction-corrected line flux, normalized to H α . Following are \log of H α luminosities in erg s^{-1} .

^a ap1.1 and ap1.2 refer to the narrow, near-systemic and broad, blueshifted emission-line components, respectively.

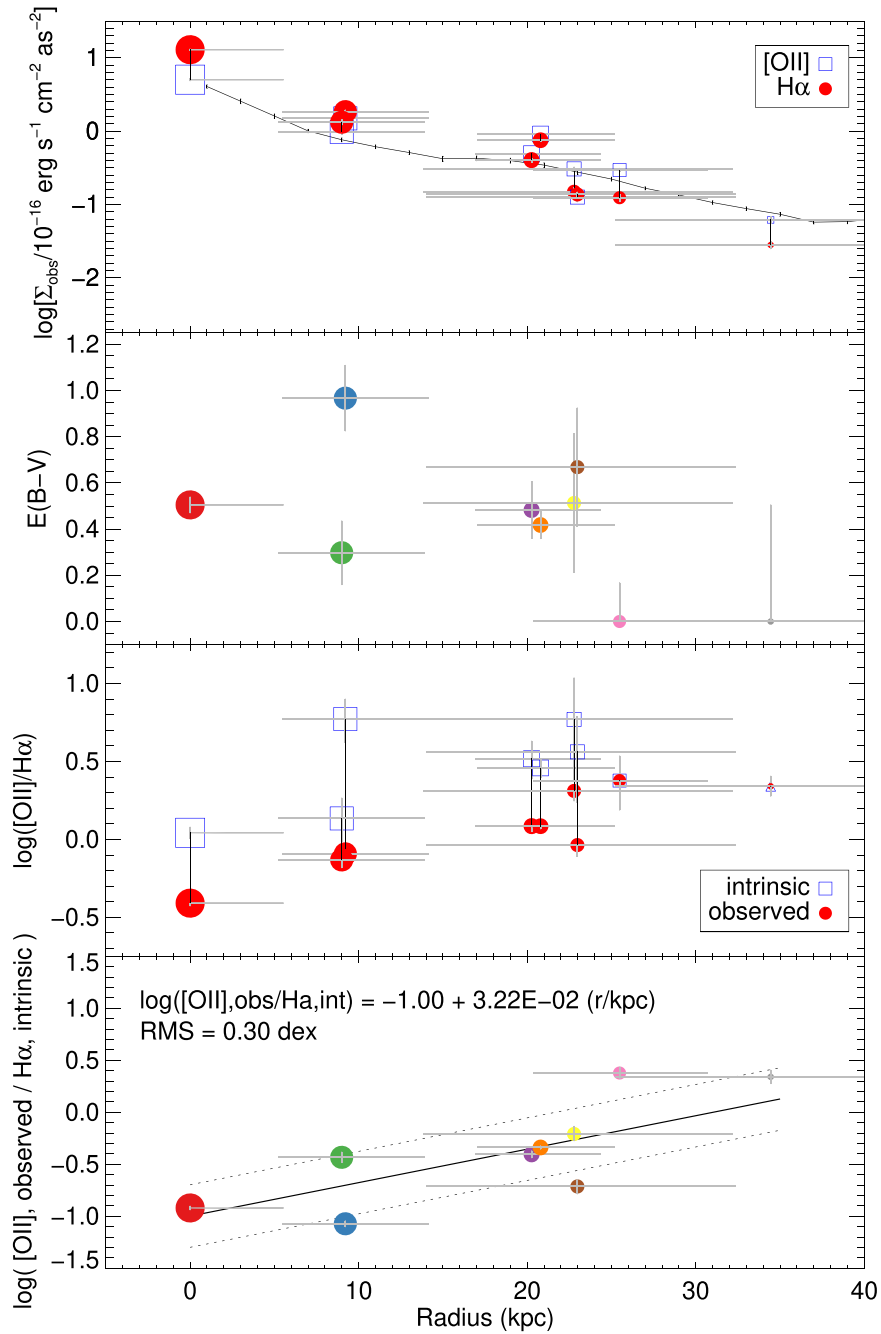


Figure 4. Top: radial dependence of observed [O II] and H α surface brightness in each spectrum. The line shows the azimuthally averaged radial surface brightness profile of [O II] measured with KCWI (Rupke et al. 2019). Each point is centered on the radius of the aperture center; horizontal gray lines are the radii spanned by each extraction aperture, and vertical gray lines are 1σ errors. Points in the same aperture are connected by vertical bars, and points at radius >0 kpc are randomly offset slightly in radius to prevent visual overlap. Top middle: color excess $E(B - V)$ vs. radius. $E(B - V)$ is computed from the Balmer decrement. Vertical error bars are 1σ . Point colors correspond to the aperture colors from Figure 1. Reddening is observed out to 20 kpc. Bottom middle: variation of observed and intrinsic [O II]/H α flux ratio with distance from the host galaxy. The final point is a lower limit owing to the large uncertainty in $E(B - V)$. Both ratios increase steadily from the host to the outskirts of the nebula. Bottom: correction from observed [O II] to intrinsic H α vs. radius. The lines show a linear fit to the data and (fit \pm rms).

optically thick, the ratio of the observed covering factors is $C_{\text{f,FeII}}/C_{\text{f,NaI}} \sim 3-4$, suggesting that Na I D is too shallow.

Second, neutral gas absorption in outflows is closely connected with the foreground dust column (Rupke & Veilleux 2015; Rupke et al. 2021). Though there is significant scatter, the observed $E(B - V) = 0.6 - 1.0$ in ap1 and ap2 (Figure 4) are typically associated with $5-10\times$ higher W_{eq} on average.

Finally, a comparison to the radial surface brightness profile of Mg II (Figure 6) shows that the Na I D surface brightness declines much more slowly than that of Mg II. If this is due to infilling of emission by foreground absorption, Na I D should intrinsically be brighter in ap1 by a factor of a few (0.6 ± 0.2 dex). This, in turn, would raise the absorption equivalent width by the same factor and the covering factor by some (smaller) amount. This reduction of Na I D flux due to

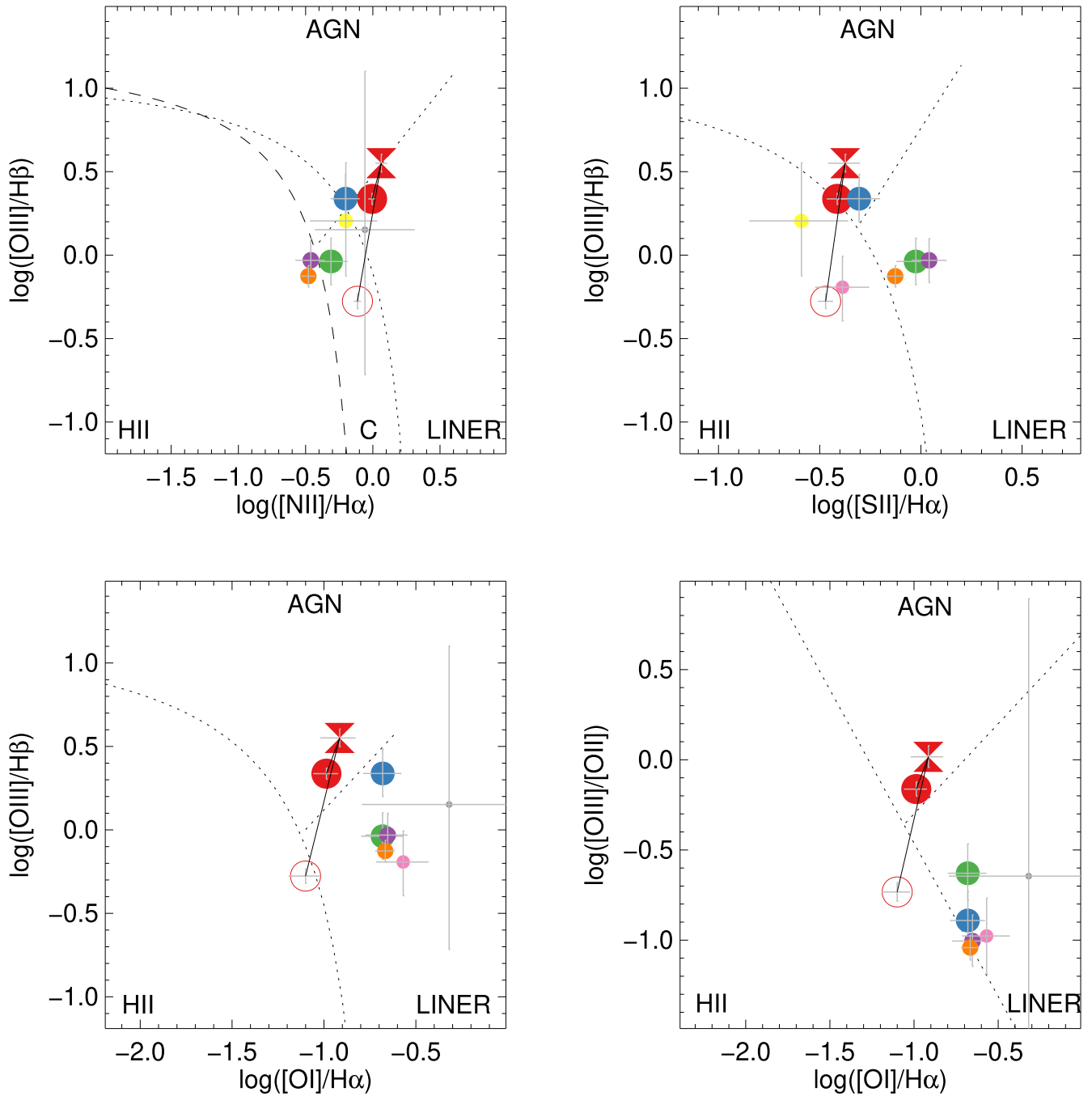


Figure 5. Excitation plots for the Makani nebula. The dashed and dotted lines divide nuclear classification regions of star-forming (H II), AGN, LINER, and composite (C) using canonical dividing lines (Kauffmann et al. 2003; Kewley et al. 2006; Cid Fernandes et al. 2010). The symbol size reflects projected distance from the host galaxy, with smaller symbols at larger radius. Filled circles are from total fluxes. The bow tie is the central aperture broad component (ap1.2), and the open circle is the corresponding narrow component (ap1.1).

infilling is observed in other spatially resolved observations (Rupke & Veilleux 2015).

Due to this infilling, we do not attempt to estimate the column density, and thus the mass and dynamics, of the neutral phase of the wind.

4. Discussion

4.1. Properties of the Star-forming Host

Makani contains a compact ($r \sim 400$ pc) stellar core (Sell et al. 2014; Rupke et al. 2019; Diamond-Stanic et al. 2021)

with a young stellar population (Rupke et al. 2019). The low-velocity component of the innermost ($r \lesssim 5.5$ kpc) aperture, ap1.1, thus contains most or all of the star formation activity. Based on the observed line ratios (Section 3.1 and Perrotta et al. 2021), this component is photoionized by the young stellar population. The $H\alpha$ luminosity of this component is 2.1×10^{42} erg s $^{-1}$ (Table 2), which is 40% of the total luminosity in ap1 (i.e., the host galaxy). We note that this luminosity, however, is larger than the difference between the total nebular luminosity (Section 3) and wind luminosity (Section 4.4). This difference

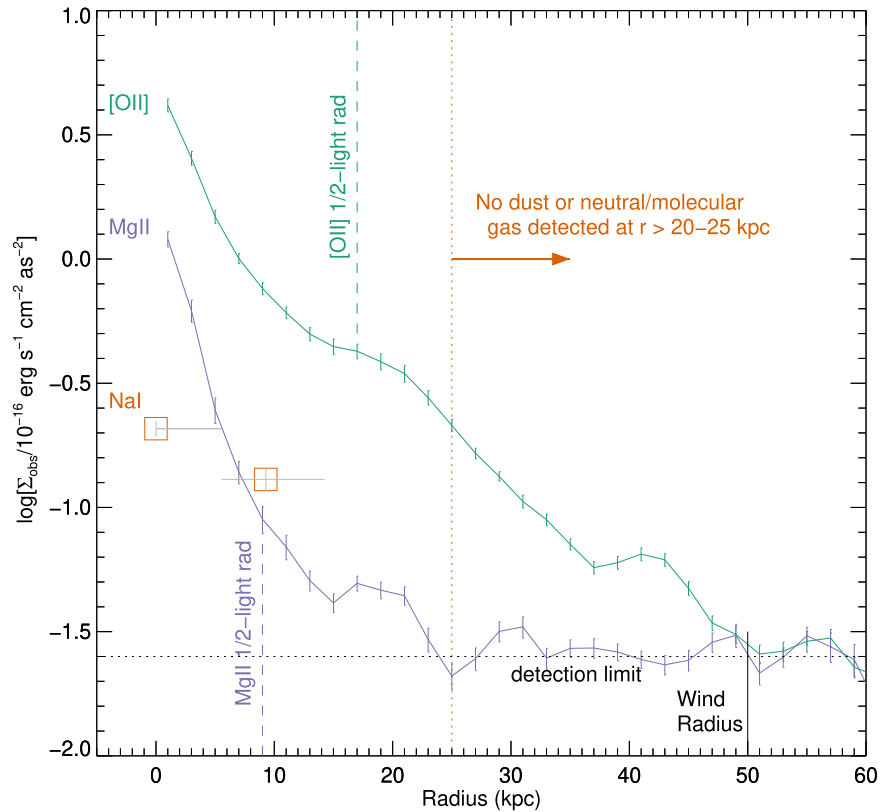


Figure 6. Radial variation of neutral gas tracers Mg II $\lambda\lambda 2796, 2803$ and Na I D in Makani. The blue line shows the azimuthally averaged radial dependence of Mg II surface brightness from KCWI data (Rupke et al. 2019), with half-light radius $r_e^{\text{Mg II}} = 9$ kpc and maximum extent 20–25 kpc. The slower decline of Na I D emission, based on the current ESI data, suggests emission-line infilling in the innermost region, reducing its flux by ~ 0.6 dex (Section 3.2). The lack of neutral/molecular gas (based on Mg II and CO from Rupke et al. 2019 and Na I from the current work) and dust (based on $E(B - V)$ from the current work; Figure 4) beyond 20–25 kpc is indicated with the vertical orange dotted line. The full extent of the ionized gas nebula from KCWI observations is shown as the solid green line, with $r_e^{[\text{O II}]} = 17$ kpc and $r_{\text{max}}^{[\text{O II}]} = 50$ kpc.

is $L_{\text{H}\alpha}^{\text{starburst}} = L_{\text{H}\alpha}^{\text{tot}} - L_{\text{H}\alpha}^{\text{wind}} = (9.4 - 8.0) \times 10^{42} \text{ erg s}^{-1} = 1.4 \times 10^{42} \text{ erg s}^{-1}$, 30% lower than the value measured from ap1.1. We take this difference as an indication of the uncertainties in our methodology, which includes assigning fluxes among the starburst and wind Episodes I and II, bootstrapping the KCWI [O II] data from the ESI measurements, and the absolute flux calibration of the current data (Section 2). In what follows we assume the average of these two values, $L_{\text{H}\alpha}^{\text{starburst}} = 1.8 \times 10^{42} \text{ erg s}^{-1}$.

Makani has an SFR of $224\text{--}300 M_{\odot} \text{ yr}^{-1}$, as inferred from radio and infrared data (Petter et al. 2020). The radio emission is concentrated in a $1''$ point source coinciding with ap1. Using a standard calibration (Moustakas et al. 2006), we compute from $L_{\text{H}\alpha}^{\text{starburst}}$ an SFR of $14 M_{\odot} \text{ yr}^{-1}$. This is a factor of 16 smaller than the lowest previous estimate from IR data. A similar discrepancy is seen in other galaxies in the parent galaxy sample of Makani (Edmonds et al. 2022). It may in fact be evidence of the stellar feedback in Makani shutting off star formation, as H α traces star formation over the shortest timescales $\lesssim 6$ Myr (Calzetti 2013). This is just below the estimated 7 Myr estimate of the most recent burst of star formation. An earlier burst occurred 400 Myr ago (Rupke et al. 2019), which is unlikely to be reflected in current SFR estimates. The observed discrepancy could also result in part from LyC leakage (Moustakas et al. 2006), to which compact starbursts with strong feedback like Makani may be susceptible (Perrotta et al. 2021).

The bright, extended Mg II emission in Makani is consistent with some LyC escape (Chisholm et al. 2020; Xu et al. 2022). The observed Mg II flux ratio in Makani, based on KCWI spectra, is $R \equiv F_{2796}/F_{2803} = 1.00 \pm 0.08$. Using the optically thin scenario, or equivalently the clumpy scenario with optically thin channels, from Chisholm et al. (2020) yields an escape fraction in the Mg II $\lambda 2796$ line of 25%. Using the line fluxes from ap1.1 in the current data and the method of Xu et al. (2022), we can make a second, independent measure of $f_{\text{esc}}(2796)$. We apply the highest-metallicity model relating the intrinsic values of [O III] $\lambda 5007$ /[O II] and Mg II $\lambda 2796$ /[O III] $\lambda 5007$ (Xu et al. 2022) to yield $F_{2796}(\text{intrinsic}) = 2.92 \times 10^{-16} \text{ erg s}^{-1} \text{ cm}^{-2}$ in the optically thin, density-bounded case. In a $1''.5$ -diameter nuclear KCWI aperture, roughly corresponding to the footprint of ap1.1, we measure $F_{2796}(\text{observed}) = 0.70 \times 10^{-16} \text{ erg s}^{-1} \text{ cm}^{-2}$. Then, $f_{\text{esc}}(2796) = F_{2796}(\text{obs})/F_{2796}(\text{int}) = 24\%$, identical to the first estimate. Comparing to observations of other Mg II emitters, this value of $f_{\text{esc}}(2796)$ suggests that $f_{\text{esc}}(\text{LyC})$ could be a few percent or higher.

Finally, it may also be the case that the bulk of the star formation is obscured by larger columns than traced by optical light, as seen in nearby compact mergers (Spoon et al. 2007). Future rest-frame far-ultraviolet and mid-infrared spectra of Makani and its parent sample could distinguish among these possibilities.

The oxygen abundance of this component is $12 + \log(\text{O}/\text{H}) \sim 9.1$ (or $\sim 2\times$ solar; Asplund et al. 2021), based on standard

[N II]/[O II] and R_{23} strong-line calibrations (Kewley & Dopita 2002). For component 1 of ap1, [N II]/[O II] = -0.12 and $R_{23} = -0.13$. This is consistent with the high mass of the galaxy (Rupke et al. 2019; Diamond-Stanic et al. 2021). The actual abundance could be closer to solar, as strong-line calibrations may overestimate the true gas abundance by a factor of ~ 2 (Kewley & Ellison 2008). The weak lines [O III] $\lambda 4363$ and [N II] $\lambda 5755$ could in principle also provide a weak-line measurement based on electron temperature. However, the inferred temperatures are much too high for high-metallicity H II regions, suggesting that component blending or simply an overestimate of the ap1.1 component in these weak lines is producing these high ratios.

4.2. Comparison to Shock Models

Line ratios are commonly used to distinguish between stellar and shock ionization in galactic winds (Lehnert & Heckman 1996; Veilleux & Rupke 2002; Sharp & Bland-Hawthorn 2010). Aside from ap1.1, the line ratios observed in Makani (Figure 5) are inconsistent with those predicted by stellar photoionization models (Kewley et al. 2001; Byler et al. 2017). An obvious place to turn instead is shock models, both due to their typical consistency with LINER-like line ratios (e.g., Dopita et al. 1997, among numerous examples) and because of the extreme outflows we detect in the Makani nebula.

We first compare the position of apertures ap3, ap4, and ap5 in Figure 5 to the low-velocity range of fast-shock models (Allen et al. 2008). We assume solar metallicity and the benchmark model preshock density $n_{\text{H}} = 1 \text{ cm}^{-3}$ (their model series M_n1). In the [N II]/H α diagram, shock velocities $v_s \sim 200 \text{ km s}^{-1}$ and low magnetic field strengths $B/n^{1/2} < 0.5 \mu\text{G cm}^{-3/2}$ can reproduce the results, whether the emission comes from the shock only or from the shock and precursor. The precursor is the gas that is about to be impacted by the shock, which in this case is fully preionized by the shock radiation. For [S II]/H α , the same low v_s and low B fit best in the shock-only grid, but the shock+precursor grid does not overlap the observed values. The [O I]/H α grids allow for shock or shock+precursor solutions, though with slightly higher velocity, $v_s \sim 250 \text{ km s}^{-1}$.

The fast-shock models cannot match the low observed ionization parameters from [O III]/[O II], even in the lower-ionization shocked region. This may point to only partial preionization of the precursor, as assumed in slow-shock models (Rich et al. 2010; Dopita & Sutherland 2017), or additional postshock physics. The slow-shock models are consistent with the observed [S II]/H α and [O I]/H α at the highest model velocities, $v_s \sim 200 \text{ km s}^{-1}$, but produce values of [N II]/H α that are too high at the same velocities.

The fast-shock models are mostly consistent with the observed values of [O II]/H $\alpha = 1 - 5$ (Figure 4). For shocked gas only, the model ratio is 2–4 for $v_s = 100\text{--}300 \text{ km s}^{-1}$, with a minimum around 200 km s^{-1} . Including the precursor, the model ratio is slightly smaller, in the 1.8–2.8 range. The observed values are much larger than those in nearby star-forming galaxies, for which the maximum observed [O II]/H α is about 2 (Moustakas et al. 2006). It is also larger than observed in the diffuse ionized gas in extraplanar regions of nearby galaxies (Jones et al. 2017).

We estimate the emitted H β fluxes, $F_{\text{H}\beta}^{\text{shock}}$, across the shock in the context of these models by dividing the luminosity in

each aperture (Table 2) by the projected physical area of each aperture in cm^{-2} (Table 1). This assumes that the shock is plane-parallel to the line of sight and so may be an underestimate if the aperture is tracing the edge of the wind. However, given the large size of the wind, projection effects are probably not significant for the inner apertures (ap1–ap5). The resulting shock fluxes $F_{\text{H}\beta}^{\text{shock}}$ in ap3–ap5 are approximately $10^{-4.0}$ to $10^{-3.7} \text{ erg s}^{-1} \text{ cm}^{-2}$. We then compare these observed fluxes to those predicted by the $Z = Z_{\odot}$ models M_n1 and V_n10 from Allen et al. (2008). We use the shock velocity and magnetic field parameter estimated from comparing the observed line ratios to the same models, $v_s = 200 \text{ km s}^{-1}$ and $B/n^{1/2} < 0.5 \mu\text{G cm}^{-3/2}$. (The result is not sensitive to B .) Finally, interpolating between the model grids, the extrapolated preshock density from fast models is then $n_{\text{H}} = 2 - 3 \text{ cm}^{-3}$, since the flux scales linearly with n_{H} (Dopita & Sutherland 1995). At larger radius, the H β fluxes decrease to the range $10^{-4.3}$ to $10^{-5.7} \text{ erg s}^{-1} \text{ cm}^{-2}$, which suggests an increase in projection effects, which means that these are lower limits, or a lower velocity and/or density at these radii. Lower velocity would be consistent, for instance, with the lower line ratios in ap6 and ap8 compared to ap3–ap5, but it seems probable that the gas density would also decrease with radius.

At $r = 0\text{--}5 \text{ kpc}$, the high-velocity outflow component ap1.2 shows elevated [O III]/H β , [N II]/H α , and [O III]/[O II] and lower [O I]/H α and [S II]/H α . The H β flux is also higher at $10^{-2.65} \text{ erg s}^{-1} \text{ cm}^{-2}$. The line ratios place this broad component in the AGN regions of the excitation diagrams. However, $n_{\text{H}} \sim 10 \text{ cm}^{-3}$ shock+precursor models from Allen et al. (2008; their models V_n10) are entirely consistent with the observed line ratios if v_s is in the range $300\text{--}400 \text{ km s}^{-1}$ and $B/n^{1/2} < 0.5 \mu\text{G cm}^{-3/2}$. These models also reproduce the observed ratios [Ne V] $\lambda 3426$ /H $\beta = -1.33 \pm 0.20 \text{ dex}$ and [Ne V] $\lambda 3426$ /[Ne III] $\lambda 3869 = -0.45 \pm 0.22 \text{ dex}$. The higher ionization state is due to the harder radiation field produced by the higher-velocity shocks. This harder radiation also produces high temperatures in the precursor and postshock regions. The observed [O III] $\lambda 4363$ / $\lambda 5007$ ratio in ap1.2 is -1.1 dex , consistent with these high temperatures ($T \gtrsim 2 \times 10^4 \text{ K}$; Section 3). Such ratios are commonly observed in LINERs (Nagao et al. 2001; Molina et al. 2018). However, the models cannot perfectly reproduce the combined [O III] $\lambda 4363$ / $\lambda 5007$ and [O III]/H β ratios, an ongoing problem (Dopita & Sutherland 1995; Allen et al. 2008).

In summary, the fast-shock models of Allen et al. (2008) are very consistent with the observed strong line ratios and fluxes throughout the nebula. In ap1.2 (the outflow at radii 0–5 kpc), high shock velocities ($300\text{--}400 \text{ km s}^{-1}$) and an ionized precursor are needed. These shock velocities align with the observed $\langle \sigma \rangle_{\text{II}} = 400 \text{ km s}^{-1}$ (Rupke et al. 2019). Farther from the host, the required shock velocities are lower, 200 km s^{-1} , but these still align with the observed line widths $\langle \sigma \rangle_{\text{I}} = 200 \text{ km s}^{-1}$. The precursor emission contributes fractionally less at these velocities. In the next section, we apply the shock models to constrain the wind density.

4.3. Shock Structure and Wind Density

We can combine the observed line flux ratios [S II] $\lambda 6716$ / $\lambda 6731$ and [O II] $\lambda 3729$ / $\lambda 3726$ with the Allen et al. (2008) shock models to constrain the ambient, preshock and postshock densities in the wind and extended nebula. The high-velocity

Episode II wind seen in ap1–ap3 has a high electron density $n_e = 3000 \text{ cm}^{-3}$ (1σ range 1200–10,000 cm^{-3}) from the [S II] ratio of ap1.2. This density is also consistent with the [O II] ratio. The shock model that best fits the observed line ratios and shock fluxes in ap1.2, ap2, and ap3 has a preshock density of $n_H \sim 10 \text{ cm}^{-3}$, as we discuss above in Section 4.2. However, compression in the shock raises the density in the postshock region up to a factor of $n_{\text{post}}/n_{\text{pre}} = (8\pi\mu m_H)^{1/2} v_{\text{shock}} / (B/n^{1/2})$ (Dopita & Sutherland 1996). For the estimated velocities of 300–400 km s^{-1} and low magnetic field parameter $0.5 \mu\text{G cm}^{-3/2}$, the maximum value of $\log(n_{\text{post}}/n_{\text{pre}})$ is 2.75. This translates to a postshock density of at most $n_{\text{post}} \sim 6000 \text{ cm}^{-3}$ for $n_{\text{pre}} = 10 \text{ cm}^{-3}$. (The compression can also be seen in Figures 3–6 of Allen et al. 2008.)

The correspondence between the observed density and predicted postshock density suggests that the observed [S II] and [O II] emission is arising primarily in the compressed postshock region. The line ratios, however, appear to require an ionized precursor. That the postshock region seems to dominate the flux of these lines could point to additional physics occurring behind the shock front, perhaps due to the accumulation of swept-up interstellar gas or to the driving mechanism of the wind.

At larger radii, in the extended, Episode I nebula, the line ratios and fluxes point to much lower ionized gas densities $n_e \lesssim 10 \text{ cm}^{-3}$. The shock models are consistent with low preshock densities of $n_H \lesssim 2\text{--}3 \text{ cm}^{-3}$, with this value possibly decreasing with increasing radius. The corresponding maximum postshock density is $n_H \lesssim 600 \text{ cm}^{-3}$. In contrast to the high-velocity, high-density Episode II gas, this implies that the [S II] ratio is primarily tracing the lower-density precursor gas. The line ratios are, for the most part, consistent with either shock-only or shock+precursor models.

The 200 and 400 km s^{-1} models with $n_H = 1\text{--}10 \text{ cm}^{-3}$ (models M_n1 and V_n10) predict that just a little over half of the H β luminosity is produced in the postshock gas, while the other fraction arises in the precursor, with little dependence on magnetic parameter $B/n^{1/2}$ (Allen et al. 2008). Thus, in the calculations that follow, we assume complete ionization in each shock region and divide the flux evenly between these low- and high-density regions. Using the estimated preshock densities and calculated maximum compression as a guideline, we assume $n_e = 10$ and 1000 cm^{-3} pre- and postshock for Episode II and $n_e = 1$ and 100 cm^{-3} for Episode I. The postshock densities could be even higher, but higher values do not significantly change the results, as the lower-density preshock gas dominates the mass.

4.4. Mass, Momentum, and Energy

As the KCWI observations did not cover strong H recombination lines, we were previously unable to measure the mass of the ionized Makani nebula. Here we use our bootstrapped estimate of the spatially resolved H α luminosity of the wind (Section 3) to estimate the mass and dynamics of both the Episode I and II winds.

We start with the Voronoi-binned, KCWI [O II] map and spatially delineate the Episode I and II winds using a velocity cut at $v_{98\%} = -700 \text{ km s}^{-1}$ (Rupke et al. 2019). To do this, we characterize multicomponent line fits in the KCWI data with the cumulative velocity distribution. We calculate velocities that enclose a particular percentage p of flux integrated from the red side of the line, $v_p\%$. (For example, $v_{98\%}$ is the velocity

at which 98% of the line flux is redshifted from this velocity and so characterizes the maximum blueshift observed.) We compute the H α flux and luminosity in each bin, applying our model for $([\text{O II}], \text{observed})/(\text{H}\alpha, \text{intrinsic})$ versus radius and using the mean radius in each Voronoi bin. From the inner $r < 5.5 \text{ kpc}$, we also conservatively remove 40% of the flux in each bin for the contribution from star-forming gas (Section 4.1).

As discussed in Section 4.3, we use the observed line ratios and shock models to infer how much of the observed luminosity arises from regions of different density. Using these luminosities and densities, we then calculate the ionized gas mass in each bin. This ionized density model differs from many estimates in the literature, which typically use only the density computed from line ratios. However, the shock models provide further information on the density structure that could yield a more accurate estimate. Given that $M^{\text{HII}} \sim n_e^{-1}$, the masses are largely dependent on the lower, preshock density in our model. This lower density is mostly consistent with the measured densities (Section 3). However, the preshock density in the Episode II shock model is lower than the density measured in the densest part of the wind, in ap1.2, by a factor of ~ 100 . Assuming a constant-density wind with the higher density measured from [S II] and [O II] in ap1.2 would result in a mass outflow rate that is lower by a similar factor.

The resulting H α luminosities and gas masses are listed in Table 3. The Episode I gas is fainter but contains more mass because of our density model. Together, the total ionized gas mass of $6.4_{-2.6}^{+5.2} \times 10^9 M_\odot$ is comparable to the integrated CO mass of $1 \times 10^{10} M_\odot$ (Rupke et al. 2019). The detected CO is much less extended than the ionized gas (reaching a radius of only 20 kpc; Figure 6). The Episode II ionized gas mass is also comparable to the CO mass of $(2.4 \pm 0.6) \times 10^9 M_\odot$ in a similar velocity range (Rupke et al. 2019).

To compute outflow rates (Table 3), we use two methods. First, we assume a single-radius wind for each episode, using $R_I = 40 \text{ kpc}$ and $R_{II} = 15 \text{ kpc}$ (Method 1). We use both the central velocity $v_{50\%}$ (Method 1a) and maximum velocity $v_{98\%}$ (Method 1b) to compute the wind properties. We deproject the velocity (either $v_{50\%}$ or $v_{98\%}$) in each bin to compute the 3D v_{rad} , using the projected galactocentric distance of the bin R_{obs} and assuming that it lies on the wind surface at the assumed 3D radius R_{wind} : $v_{\text{rad}} = v_{\text{obs}} / \cos[\sin^{-1}(R_{\text{obs}}/R_{\text{wind}})]$. We then compute the ballistic flow time for each bin, $t_{\text{flow}} = R_{\text{wind}}/v_{\text{rad}}$, and divide the mass in that bin by t_{flow} . We follow a similar procedure for momentum and energy, adding in velocity dispersion for energy (following Rupke et al. 2005).

As an alternative method, we assume that the stellar population ages t_* for Episodes I and II, 400 and 7 Myr, represent the times when all of the gas in each episode left the starburst (Method 2). We then divide the ionized mass by these times for each episode to compute $dM/dt = M/t_*$. This method is effectively a time-averaged outflow rate, where the time average is over the lifetime of the outflow. We use it as a sanity check on Method 1.

For Episode I, Method 1a (using $v_{50\%}$) yields a result consistent with Method 2, as the mean deprojected radial velocity $\langle v_{\text{rad}} \rangle = 98 \text{ km s}^{-1}$ is close to the velocity inferred from $R_I/t_{*,I} = 40 \text{ kpc}/400 \text{ Myr} = 97 \text{ km s}^{-1}$. In other words, most of the gas is at a velocity consistent with the outer radius of the nebula and the ballistic flow velocity, if this gas left the starburst 400 Myr ago. The gas that began at higher velocity

Table 3
Ionized Wind Properties

Ep	Method	$L_{\text{H}\alpha}^{\text{wind}}$ (erg s^{-1})	M (M_{\odot})	$\langle v_{\text{rad}} \rangle$ (km s^{-1})	dM/dt ($M_{\odot} \text{ yr}^{-1}$)	p (dyn s)	dp/dt (dyn)	E (erg)	dE/dt (erg s^{-1})
(1)	(2)	(3)	(4)	(5)	(6)	(7)	(8)	(9)	(10)
I	1a	$(2.25_{-1.13}^{+2.25})E + 42$	5.09E+09	98	9.8	7.59E+49	6.92E+33	6.90E+57	4.23E+41
I	1b	2.25E+42	5.09E+09	622	64.8	5.04E+50	2.45E+35	2.16E+58	1.58E+43
I	2	2.25E+42	5.09E+09	97	12.7
II	1a	$(5.75_{-1.76}^{+3.52})E + 42$	1.30E+09	157	9.2	2.70E+49	1.55E+34	7.27E+57	2.55E+42
II	1b	5.75E+42	1.30E+09	2279	151.4	4.42E+50	2.55E+36	6.59E+58	8.77E+44
II	2	5.75E+42	1.30E+09	2091	185.8

Note. Properties of the ionized wind for each episode are listed for three different methods of calculation, as described in Section 4.4. Methods 1a and 1b make use of the outflow dynamical timescale to calculate the mass, momentum, and energy outflow rates, while method 2 is based on the stellar population ages for Episodes I and II. For Episode I, we assume a wind radius $R_I = 40$ kpc, electron density $n_e = 1\text{--}100 \text{ cm}^{-3}$, and time when the wind left the starburst (for Method 2) equal to the stellar population age $t_{*,I} = 400$ Myr. For Episode II, we assume $R_{II} = 15$ kpc, $n_e = 10\text{--}1000 \text{ cm}^{-3}$, and $t_{*,II} = 7$ Myr. We also remove 40% of the flux at $r < 5.5$ kpc to conservatively account for star formation in the inner nebula (Section 4.1), which is equivalent to removing $1.4 \times 10^{42} \text{ erg s}^{-1}$ from Episode II. Our preferred methods are 1a and 2 for Episode I and 1b and 2 for Episode II. The 1σ errors propagated from our bootstrapping method (Section 3) are included for $L_{\text{H}\alpha}$, and similar fractional errors apply to other quantities calculated from $L_{\text{H}\alpha}$. Systematic errors due to our choice of density model, etc., are not included.

has either slowed or since escaped to much larger radius. The remaining detected amounts of high-velocity gas do not contribute significantly to the mass, or mass outflow rate, of the outflow. Using $v_{98\%}$ to trace the radial velocity of the bulk of the gas thus overestimates the flow rate.

For Episode II, Method 1b (using $v_{98\%}$) is consistent with Method 2, due again to comparable $\langle v_{\text{rad}} \rangle = 2279 \text{ km s}^{-1}$ and $R_{II}/t_{*,II} = 15 \text{ kpc}/7 \text{ Myr} = 2091 \text{ km s}^{-1}$. Method 1a, in contrast, yields a flow rate $15\times$ lower. In this case, while the fastest gas has flowed to the largest observed radius, the lower-velocity gas has not had time to do so. Thus, the assumption of a single radius for the inner wind is probably incorrect, and a flow rate computed from the flow time in each spaxel, t_* (i.e., Method 2), is more correct. This interpretation implies that the inferred radius, $R_{II} = v_{\text{rad}}/t_{*,II}$, is velocity dependent. Lower-velocity spaxels will have smaller radius, and our single-radius deprojection will underestimate the radial velocity. For both of these reasons, Method 1a produces a significant underestimate for the Episode II wind.

We conclude that Methods 1a and 2 are closer to the correct flow rates for Episode I, while Methods 1b and 2 are closer to the correct flow rates for Episode II. The inferred mass outflow rates are thus in the range $10\text{--}13 M_{\odot} \text{ yr}^{-1}$ for Episode I and $151\text{--}186 M_{\odot} \text{ yr}^{-1}$ for Episode II. Again, dM/dt_{II} for the ionized gas is comparable to the CO value, $245 M_{\odot} \text{ yr}^{-1}$. In most nearby compact starbursts, dM/dt in the ionized gas is much smaller than in the molecular gas, though with significant scatter (e.g., Rupke & Veilleux 2013; Fluetsch et al. 2021). However, the canonical density model in these calculations is inferred from optical line ratios; we combine the line ratio densities with the shock model density structure, which raises the inferred masses. In Perrotta et al. (2023), we show that measurements of dM/dt from Mg II and Fe II absorption lines in other compact starbursts from the Tremonti et al. (2007) sample are consistent with mass outflow rates of order $10^2\text{--}10^3 M_{\odot} \text{ yr}^{-1}$.

Note that we choose the single wind radius for each episode based on two factors. The first is the observed wind morphology (Rupke et al. 2019). We refine the radius to approximately match the average deprojected velocity $\langle v_{\text{rad}} \rangle$ and the velocity R/t_* for the two methods (1a or 1b and 2) that

produce the best agreement in dM/dt for each episode. The resulting dM/dt is not sensitive to a 30% change in R_{wind} .

4.5. Powering the Nebula and Driving the Wind

We have shown that the line emission from the wind is most consistent with shock models (Section 4.2). We nonetheless consider whether the radiative energy from the starburst is capable of powering the $\text{H}\alpha$ luminosity of the nebula.

We first assume the current SFR as given by IR/radio tracers, rather than $\text{H}\alpha$. A $\lesssim 6.5$ Myr instantaneous burst or a $\gtrsim 7$ Myr continuous burst with SFR of $224\text{--}300 M_{\odot} \text{ yr}^{-1}$ produces $Q(\text{H}^0) = (1.9\text{--}2.6) \times 10^{55}$ ionizing photons s^{-1} (Leitherer et al. 1999). The ratio of $\text{H}\alpha$ photons to ionizing photons is $\alpha_{\text{H}\alpha}^{\text{eff}}/\alpha$, or the ratio of the effective to total recombination coefficients. For case B at $T = 10^4$ K and $n_e = 100 \text{ cm}^{-3}$, $\alpha_{\text{H}\alpha}^{\text{eff}}/\alpha_B = \alpha_{\text{H}\beta}^{\text{eff}}/\alpha_B \times (j_{\lambda} \lambda)_{\text{H}\alpha}/(j_{\lambda} \lambda)_{\text{H}\beta} = 0.452$, where j_{λ} are the line emissivities and we use the emissivity and recombination coefficient tabulations of Hummer & Storey (1987). This yields an $\text{H}\alpha$ luminosity predicted from the radio/IR SFR of $L_{\text{H}\alpha}^{\text{SFR}} = (2.6\text{--}3.5) \times 10^{43} \text{ erg s}^{-1}$, which is $3\text{--}4\times$ larger than the observed luminosity of the nebula, $L_{\text{H}\alpha}^{\text{tot}}(\text{H}\alpha) = 9.4 \times 10^{42} \text{ erg s}^{-1}$ (Section 3).

Photoionizing the entire nebula would require a significant fraction of the LyC to leak outside of the inner starburst region. We can infer from the predicted $\text{H}\alpha$ luminosity $L_{\text{H}\alpha}^{\text{SFR}}$ and the $\text{H}\alpha$ emission attributed to the starburst, $L_{\text{H}\alpha}^{\text{starburst}} = 1.8 \times 10^{42} \text{ erg s}^{-1}$ (Section 4.1), that a fraction $L_{\text{H}\alpha}^{\text{starburst}}/L_{\text{H}\alpha}^{\text{SFR}} \sim 0.05\text{--}0.07$ of the LyC is required to ionize the gas consistent with stellar photoionization (ap1.1). To energize the $\text{H}\alpha$ emission in the wind ($L_{\text{H}\alpha}^{\text{wind}} = 8.0 \times 10^{42} \text{ erg s}^{-1}$; Table 3) would require an additional 23%–31% of the LyC emitted by the starburst. The total escape fractions for the inner starburst and entire nebula, respectively, would then be of order 90% and 65%, which are uncomfortably high for a galaxy of this mass and ionization parameter (Izotov et al. 2022). Thus, if the nebula were photoionized by the starburst rather than shocks, significant absorption of LyC by dust or a very recent SFR that is much lower would be necessary (Section 4.1).

The shock models also make energetic predictions about the total flux radiated in the shocks to which we can compare the data. The mechanical energy flux that powers the shock is

completely radiated by the cooling gas (Dopita & Sutherland 1996). Assuming $H\alpha/H\beta = 2.86$, the ratio of the total radiated luminosity L_{rad} to the observed $H\alpha$ luminosity is given by (Dopita & Sutherland 1995)

$$\frac{L_{\text{shock}}}{L_{H\alpha}} = 107 v_{s,100}^{0.59} (1 + 1.32 v_{s,100}^{-0.13})^{-1}, \quad (1)$$

where $v_{s,100}$ is the shock velocity in units of 100 km s^{-1} .

Here we compare the energy produced in the shocks to the mechanical energy observed in the warm, ionized and molecular phases of the wind episodes. We also look at how the mass, momentum, and energy in the wind could arise from the starburst itself.

4.5.1. Episode II Ionized Wind

The best-fitting model shock velocity is $v_s = 400 \text{ km s}^{-1}$, which yields $L_{\text{shock,II}} = 115 L_{H\alpha,II}^{\text{wind}} = 6.6 \times 10^{44} \text{ erg s}^{-1}$. If we assume, based on their similar mass and dynamics, that the ionized and molecular components of the fast wind contribute similarly to the energy flow rate dE/dt , then $dE/dt_{\text{II}}^{\text{HII}+\text{H}_2} = 1.8 \times 10^{45} \text{ erg s}^{-1} = 2.7 L_{\text{shock,II}}$. In other words, the inferred mechanical energy in the ionized and molecular components of the wind is capable of powering the total radiated luminosity in the shock models.

The mechanical energy produced by the starburst is probably less than both of these numbers. Assuming a continuous starburst of age $t_{*,\text{II}}$, solar metallicity, and a Salpeter initial mass function with stellar masses $M = 0.1\text{--}100 M_{\odot}$, Starburst99 predicts a mechanical luminosity in the hot ejecta of $dE/dt_* = 2.4 \times 10^{43} \text{ erg s}^{-1}$ (Leitherer et al. 1999). Because of the relatively young age of this starburst, some supernovae have not yet released their energy. So older, continuous bursts would contain a greater fraction of the asymptotic value of dE/dt_* , which is $\sim 8 \times 10^{43} \text{ erg s}^{-1}$ for $\text{SFR} = 300 M_{\odot} \text{ yr}^{-1}$. Even if we assume that 100% of this mechanical energy is thermalized into hot ejecta that then drives the outflow, the range of possible dE/dt_* is $\lesssim 4\%$ of $dE/dt_{\text{II}}^{\text{HII}+\text{H}_2}$.

An alternative to being driven by the energy in the hot ejecta from the central starburst is that the Makani wind is driven by the mechanical and radiative momentum of the burst. Compact starbursts with strong winds, like Makani, are prime candidates for outflows driven by the radiation pressure from Eddington-limited star formation (Murray et al. 2005; Thompson et al. 2005; Diamond-Stanic et al. 2012). The momentum in the stellar winds and supernova ejecta from the starburst is $dp/dt_* = \sqrt{2} dM/dt_* dE/dt_*$ (Veilleux et al. 2020). The input mass-loss rate from the hot ejecta is $dM/dt_* \sim 12 M_{\odot} \text{ yr}^{-1}$ (Leitherer et al. 1999), so that $dp/dt_* = 1.9 \times 10^{35} \text{ dyn}$. However, observations of the hot wind ejecta in M82 suggest that $dM/dt_* = (0.1\text{--}0.3)\text{SFR}$ (Strickland & Heckman 2009), depending on the mass loading of the hot wind by cold clouds within the starburst region. This would imply $dM/dt_* \sim 30\text{--}90 M_{\odot} \text{ yr}^{-1}$, and in turn $dp/dt_* = (3\text{--}5) \times 10^{35} \text{ dyn}$. For the calculations below, we take the midpoint of this range, $4 \times 10^{35} \text{ dyn}$.

The input from radiation pressure is $dp/dt_{\text{rad}} = (1 + \tau_{\text{eff,IR}})L_{\text{bol}}/c$, assuming an optically thick wind, where $\tau_{\text{eff,IR}}$ is the effective far-infrared optical depth and accounts for multiple photon scatterings (Thompson et al. 2015; Veilleux et al. 2020). For Makani, $dp/dt_{\text{rad}} = (1 + \tau_{\text{eff,IR}})3.8 \times 10^{35} \text{ dyn}$, based on $L_{\text{bol}} \sim 2L_{\text{IR}} = (1.16 \pm 0.18) \times 10^{46} \text{ erg s}^{-1}$ (Petter et al. 2020).

We find $dp/dt_{\text{II}}^{\text{HII}+\text{H}_2} = 7 \times (dp/dt_* + dp/dt_{\text{rad}})$ for $\tau_{\text{eff,IR}} = 0$. A similar momentum “boost” is commonly observed in molecular AGN outflows (Sturm et al. 2011; Cicone et al. 2014; González-Alfonso et al. 2017); in that context, the boost is defined as $(dp/dt)/(L/c)$. Boosts $(dp/dt)/(dp/dt_*) = 1\text{--}10$ are common in the warm, ionized outflows of $10\text{--}100 M_{\odot} \text{ yr}^{-1}$ starbursts (Heckman et al. 2015). As we discuss above, the energy delivered by the starburst hot ejecta may be insufficient to drive the wind. The bulk momentum dp/dt_* of the hot wind may be transferred to the cold clouds, but additional momentum can come from work done by the expanding hot bubble during its energy-conserving phase of expansion (Lochhaas et al. 2018; Veilleux et al. 2020). The maximum momentum of a wind powered by a single-phase, radiatively cooling hot wind is also predicted to be several times higher than the estimate of dp/dt_* based on M82, at $1.2 \times 10^{36} \text{ dyn}$ (Lochhaas et al. 2021). When combined with the momentum from radiation pressure, this is only a factor of two below the observed momentum flow rate of the wind. Finally, $\tau_{\text{eff,IR}} \gg 1$ (i.e., many photon scatterings) could in principle contribute significantly to driving the wind (Zhang & Davis 2017; though see also Menon et al. 2022). This would be consistent with the dusty, molecular+neutral phase observed in the Episode II flow (Section 4.6).

The gravitational potential of the galaxy will work to decelerate this flow. At a radius of 10 kpc, $F_{\text{grav}} \sim 1 \times 10^{35} \text{ dyn}$ for the $4 \times 10^9 M_{\odot}$ of outflowing molecular and ionized gas we observe. Thus, gravity is not significantly decelerating the fast, Episode II wind. Since $F_{\text{grav}} \propto M_{\text{wind}}/r^2$, at smaller radius the wind may have experienced significant deceleration, but it also may have entrained much less material at earlier times.

Momentum is certainly flowing from the hot to the cool wind. A substantial fraction of the cool, outflowing phase thus arises from clouds that are accelerated by the hot phase. The cool clouds may also acquire mass directly from the hot wind and CGM surrounding the galaxy. The hot wind can transfer mass to the cold phase via radiative cooling (Thompson et al. 2016) and/or turbulent mixing at cloud boundaries (Gronke & Oh 2018, 2020; Fielding et al. 2020; Schneider et al. 2020).

The mass outflow rate in the Episode II wind implies significant entrainment of cool gas, in that the ratio of mass flowing out in the cool, ionized and molecular wind is many times the mass predicted to be in the hot wind originating in the starburst. Using the values of dM/dt_* from Strickland & Heckman (2009) that assume some mass loading of the hot ejecta from stellar winds and supernovae within the starburst injection zone (see above), $(dM/dt_{\text{II}}^{\text{HII}+\text{H}_2})/(dM/dt_*) = 5\text{--}15$. The mass outflow rate is also larger than the SFR: $dM/dt_{\text{II}}^{\text{HII}+\text{H}_2} \sim 1.4 \text{ SFR}$ for $\text{SFR} = 300 M_{\odot} \text{ yr}^{-1}$. This value of $(dM/dt_{\text{II}})/\text{SFR}$ is consistent with other measurements of star-forming galaxies of similar mass (Heckman et al. 2015), which range from 0.3 to 3. Though the $(dM/dt_{\text{II}})/(dM/dt_*)$ ratio is conceptually closer to representing the mass loading of the hot wind with cool clouds, the ratio $(dM/dt_{\text{II}})/\text{SFR}$ is also called the “mass-loading factor.” The degree of cold cloud entrainment in analytic two-phase models then points to large initial cloud sizes $M_{\text{cl}} \gtrsim 10^5\text{--}10^6 M_{\odot}$ in the Makani wind, such that the cooling time is short compared to the mixing time (Fielding & Bryan 2022). It also implies that the large observed cool cloud “mass loading” of $(dM/dt_{\text{II}})/\text{SFR} \sim 1.4$ is not, in fact, too large to cause the wind to stall, as suggested by some energy-driven models (Thompson et al. 2016; Fielding &

Bryan 2022). This is probably consistent with the need for significant radiation pressure driving of the cool wind.

This mixing of mass and energy between the cool and hot phases could also be an alternative power source for the ionized nebular emission. In the single-phase analytic model of Thompson et al. (2016), the hot wind cools radiatively as it expands into the galaxy, and then again as it shocks with the surrounding CGM. By contrast, in the explicitly multiphase analytic model of Fielding & Bryan (2022), the cool phase exists even at the base of the wind. The multiphase wind carries millions of $n \lesssim 10 \text{ cm}^{-3}$ clouds that are area filling (though not volume filling). The cooling gas in the cloud boundary layer between the hot and cool phases, with $T = 0.2 - 1 \times 10^5 \text{ K}$, then produces line emission in the wind.

Increasing n_e in the ionized gas, so that all of the $\text{H}\alpha$ emission arises in the compressed, postshock region (Section 4.3), would lower the mass, momenta, and energy in the ionized gas by a factor ~ 50 . This would reduce the observed momentum boost and mass-loading factor. However, the fact would remain that the mass, momentum, and energy in the molecular gas are still at the level shown in Table 3 for Episode II, so that the total flow rates would only decrease by a factor of 2. Furthermore, the large flow rates we observe are consistent with those measured in the neutral and ionized phase of similar galaxies via other probes (Perrotta et al. 2023).

4.5.2. Episode I Ionized Wind

The Episode I ionized wind, with $v_s = 200 \text{ km s}^{-1}$, has an estimated ionized mass $M_I \sim 4M_{II}$. This mass may be distributed over a much larger volume, however: $[(R_I/R_{II})^3 - 1] \sim 15$. The outflow rate in Episode I is also more than $10\times$ smaller. As discussed above, high-velocity gas from Episode I may have carried significant amounts of mass beyond $r_{\text{wind}} = 50 \text{ kpc}$, further into the CGM. Alternatively, the wind may simply have slowed down in the extended halo/CGM of the galaxy, reducing dM/dt while still entraining more gas at larger radius (Lochhaas et al. 2018). Consistent with this possibility is the observation that the outflow velocity in the parent sample of Makani decreases with increasing light-weighted age (Davis et al. 2022, submitted). In Episode II, some or all of the cool wind arose from the host galaxy, originating in cool clouds or condensed from the hot wind. However, much more of the mass entrainment at larger radii may be due to radiative cooling and/or turbulent mixing from the hot wind and/or CGM (Thompson et al. 2016; Gronke & Oh 2018; Fielding et al. 2020).

The radiated energy in the Episode I shocks is $L_{\text{shock,I}} = 73L_{\text{H}\alpha,\text{I}} = 1.6 \times 10^{44} \text{ erg s}^{-1}$. For Episode I, we include only the ionized gas, since the CO gas is contained in the Episode II footprint. Thus, $dE/dt_{\text{I}}^{\text{HII}} = 0.003L_{\text{shock,I}}$, a significant discrepancy. We conclude that much of the energy in the shocks beyond $r \sim 20 \text{ kpc}$ must come from the mechanical energy of a different phase of the outflow. This could be the hot phase traced by higher ionization states like O VI, as observed in the CGM in absorption at large impact parameters (e.g., Tumlinson et al. 2011). Shocks may in fact arise naturally in the interaction between a hot wind and surrounding CGM (Thompson et al. 2016).

4.6. Episode II Dusty Wind

Observations of molecular gas and $\text{Mg II } \lambda\lambda 2796, 2803$ emission to radii 20–25 kpc point to the presence of significant H I and H₂ in the inner, Episode II wind. The presence of these two tracers also indicates significant amounts of dust out to similar radii. However, these dusty gas phases appear only at the inner edge of the Episode I wind (Rupke et al. 2019).

Two new lines of evidence confirm this picture. First, Na I D is detected in two apertures out to $r = 10\text{--}15 \text{ kpc}$ (Figure 6). The presence of Na I D has long been closely associated with dust extinction (see, e.g., Rupke et al. 2021, and references therein), due to dust being required to keep Na in the neutral phase. Second, we detect substantial gas extinction, $E(B - V) \sim 0.5$, out to $r = 20\text{--}25 \text{ kpc}$ (Figure 4).

Such dusty, neutral outflows on $\sim 10 \text{ kpc}$ scales are commonly observed in compact starbursts in nearby mergers (Rupke & Veilleux 2013). Frequently, high spatial resolution observations show filamentary dust structures associated with these outflows. Future high-resolution observations of Makani with the James Webb Space Telescope may resolve these dust structures, as well as more directly determine the radial extent of dust in the wind.

5. Conclusion

The giant Makani galactic wind is driving ionized, neutral, and molecular gas and dust out of a compact starburst into the CGM. In the preceding sections we have presented a spatially resolved analysis of the physical state and mass, momentum, and energy in the ionized phase of the wind using rest-frame optical spectra. These ionization and dynamical measurements are key to unlocking the driving force of the Makani wind, as well as its impact on and interaction with the surrounding CGM.

The fast, inner wind extending to $R_{II} = 20 \text{ kpc}$ —Episode II—is powered by a young starburst of age 7 Myr (Rupke et al. 2019) and SFR $224\text{--}300 M_{\odot} \text{ yr}^{-1}$ (Petter et al. 2020). Using line ratios and the luminosity of recombination lines, we conclude that the ionized gas in the inner wind is energized by fast, $v_s = 400 \text{ km s}^{-1}$ shocks moving through a low-density $n_{\text{H}} \sim 10 \text{ cm}^{-3}$ medium (Allen et al. 2008), consistent with earlier results (Perrotta et al. 2021). The velocity dispersion of the gas is equal to this model shock velocity: $\langle \sigma \rangle_{II} = 400 \text{ km s}^{-1}$. The shock compresses this gas to high density, yielding $n_e \gtrsim 10^3 \text{ cm}^{-3}$ in the postshock region. The hard radiation field of the shock produces high-ionization line emission commonly seen in AGNs ([Ne V] $\lambda 3426$), as well as high gas temperatures $T > 2 \times 10^4 \text{ K}$, as traced by [O III] $\lambda 4363$ and [N II] $\lambda 5755$.

Molecular and neutral gas was previously detected throughout the Episode II wind (Rupke et al. 2019). We find new evidence for neutral, dusty gas in the wind in the form of Na I D absorption in the host galaxy and emission out to 10–15 kpc and extinction in the ionized gas, as traced by the Balmer decrement, to 20–25 kpc.

A much older and larger wind, extending from $R_I = 20$ to 50 kpc—Episode I—was powered by a star formation event 400 Myr ago (Rupke et al. 2019). Currently, only ionized gas is detected in the Episode I wind, and it is energized by 200 km s^{-1} shocks in $n_{\text{H}} \lesssim 2\text{--}3 \text{ cm}^{-3}$ gas. Again, this is

consistent with the observed velocity dispersion of this outflow, $\langle\sigma\rangle_I = 200 \text{ km s}^{-1}$ (Rupke et al. 2019).

Using measurements of [O II] $\lambda\lambda 3726, 3729$ and $\text{H}\alpha$ throughout the wind, we model the radial dependence of their ratio. We apply this model to the fully spatially resolved [O II] map of the nebula to compute $L_{\text{H}\alpha}$ across the full nebula. We then combine the shock structure predicted by models (Dopita & Sutherland 1996; Allen et al. 2008) with the density from line ratios to measure the mass in each wind episode. Finally, we employ three different methods for computing dM/dt , p , dp/dt , E , and dE/dt in the ionized wind from the 2D mass and velocity maps of the nebula.

Our preferred model of the Episode II nebula is a massive, powerful, ionized wind that is comparable to that of the molecular phase, with $M_{\text{II}}^{\text{HII}} \sim M_{\text{II}}^{\text{H}_2} = (1 - 2) \times 10^9 M_{\odot}$ and $dM/dt_{\text{II}}^{\text{HII}} \sim dM/dt_{\text{II}}^{\text{H}_2} = 170\text{--}250 M_{\odot} \text{ yr}^{-1}$. Together, the ionized and molecular phases are depleting gas from the galaxy at $1.4\times$ the SFR. These phases carry as much energy as is predicted to be fully radiated by the shocked gas (Dopita & Sutherland 1995). They need significantly more momentum than is initially contained in the hot ejecta from the recent starburst, with a required boost of ~ 7 . We suggest that radiation pressure from an Eddington-limited starburst is a likely culprit (Diamond-Stanic et al. 2012; Thompson et al. 2015), on top of the momentum produced by the hot wind (Thompson et al. 2016; Lochhaas et al. 2021; Fielding & Bryan 2022).

The slower, Episode I wind has a much lower outflow rate of $dM/dt_I^{\text{HII}} \sim 10 M_{\odot} \text{ yr}^{-1}$. However, this ionized wind has moved into the galaxy's CGM and is depositing gas in a much larger volume. It contains even more ionized gas; in our density model, $M_I^{\text{HII}} = 5 \times 10^9 M_{\odot}$. This increase in mass as the wind slows but moves to larger radius may be due to loading from radiative cooling of the hot wind or CGM and/or mixing of the hot gas into the cool phase through mixing layers (Lochhaas et al. 2018; Fielding et al. 2020; Gronke & Oh 2020). The gas may also be shocking on the surrounding CGM (Thompson et al. 2016). The energy contained in this flow is quite small, however, compared to the flux predicted to be radiated in the shocked gas, with $dE/dt_I = 0.003L_{\text{shock},I}$. Thus, much of the energy and momentum in Episode I may be carried in a hotter phase. Alternatively, significant energy from the fastest-moving gas in the earlier wind may simply have escaped to large radius.

The clearest way to make progress on the Makani wind and its connection to the CGM will be to try to detect hot gas in the extended nebula and measure its mass and energy content. This could be in the form of deep X-ray observations or UV observations of ionization states like O VI. On the other side of the energetic spectrum, the dusty, neutral phase is detected to 20–25 kpc, but its physical conditions are mostly unknown. Deep mid-infrared imaging and spectroscopy with the JWST would produce much stronger constraints on its presence and properties in both wind episodes. Finally, we could reduce uncertainties in the present work through integral field maps of the recombination lines in Makani with wide-field, red-sensitive instruments like the Multi Unit Spectroscopic Explorer (MUSE) or the Keck Cosmic Reionization Mapper (KCRM).

We thank Drummond Fielding and Cassi Lochhaas for insights into recent wind models and Sylvain Veilleux for comments on the manuscript. We acknowledge support from

the National Science Foundation (NSF) under a collaborative grant (AST-1813299, 1813365, 1814233, 1813702, and 1814159). S.P. and A.L.C. acknowledge support from the Heising-Simons Foundation grant 2019–1659.







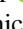
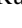

The data presented herein were obtained at the W. M. Keck Observatory, which is operated as a scientific partnership among the California Institute of Technology, the University of California, and the National Aeronautics and Space Administration. The Observatory was made possible by the generous financial support of the W. M. Keck Foundation.

The authors wish to recognize and acknowledge the very significant cultural role and reverence that the summit of Maunakea has always had within the indigenous Hawaiian community. We are most fortunate to have the opportunity to conduct observations from this mountain.

Facility: Keck:II (ESI) .

Software: ESIRedux (<https://www2.keck.hawaii.edu/inst/esi/ESIRedux/index.html>); IFSFIT (Rupke 2014).

ORCID iDs

David S. N. Rupke  <https://orcid.org/0000-0002-1608-7564>
 Alison L. Coil  <https://orcid.org/0000-0002-2583-5894>
 Serena Perrotta  <https://orcid.org/0000-0002-2451-9160>
 Ryan C. Hickox  <https://orcid.org/0000-0003-1468-9526>
 John Moustakas  <https://orcid.org/0000-0002-2733-4559>
 Grayson C. Petter  <https://orcid.org/0000-0001-6941-8411>
 Gregory H. Rudnick  <https://orcid.org/0000-0001-5851-1856>
 Paul H. Sell  <https://orcid.org/0000-0003-1771-5531>
 Kelly E. Whalen  <https://orcid.org/0000-0002-8571-9801>

References

- Allen, M. G., Groves, B. A., Dopita, M. A., Sutherland, R. S., & Kewley, L. J. 2008, *ApJS*, **178**, 20
- Asplund, M., Amarsi, A. M., & Grevesse, N. 2021, *A&A*, **653**, A141
- Baldwin, J. A., Phillips, M. M., & Terlevich, R. 1981, *PASP*, **93**, 5
- Bordoloi, R., Tumlinson, J., Werk, J. K., et al. 2014, *ApJ*, **796**, 136
- Byler, N., Dalcanton, J. J., Conroy, C., & Johnson, B. D. 2017, *ApJ*, **840**, 44
- Calzetti, D. 2013, in *Secular Evolution of Galaxies*, ed. J. Falc3n-Barroso & J. H. Knapen (Cambridge: Cambridge Univ. Press), 419
- Cappellari, M. 2012, pPXF: Penalized Pixel-Fitting stellar kinematics extraction, *Astrophysics Source Code Library*, ascl:1210.002
- Cappellari, M. 2017, *MNRAS*, **466**, 798
- Cardelli, J. A., Clayton, G. C., & Mathis, J. S. 1989, *ApJ*, **345**, 245
- Chisholm, J., Prochaska, J. X., Schaerer, D., Gazagnes, S., & Henry, A. 2020, *MNRAS*, **498**, 2554
- Cicone, C., Maiolino, R., Sturm, E., et al. 2014, *A&A*, **562**, A21
- Cid Fernandes, R., Stasińska, G., Schlickmann, M. S., et al. 2010, *MNRAS*, **403**, 1036
- Diamond-Stanic, A. M., Moustakas, J., Sell, P. H., et al. 2021, *ApJ*, **912**, 11
- Diamond-Stanic, A. M., Moustakas, J., Tremonti, C. A., et al. 2012, *ApJL*, **755**, L26
- Dopita, M. A., Koratkar, A. P., Allen, M. G., et al. 1997, *ApJ*, **490**, 202
- Dopita, M. A., & Sutherland, R. S. 1995, *ApJ*, **455**, 468
- Dopita, M. A., & Sutherland, R. S. 1996, *ApJS*, **102**, 161
- Dopita, M. A., & Sutherland, R. S. 2017, *ApJS*, **229**, 35
- Edmonds, K., Jones, N., Edgar, S., et al. 2022, *AAS Meeting*, **54**, 241.50
- Fielding, D. B., & Bryan, G. L. 2022, *ApJ*, **924**, 82
- Fielding, D. B., Ostriker, E. C., Bryan, G. L., & Jermyn, A. S. 2020, *ApJL*, **894**, L24
- Fluetsch, A., Maiolino, R., Carniani, S., et al. 2021, *MNRAS*, **505**, 5753
- Geach, J. E., Hickox, R. C., Diamond-Stanic, A. M., et al. 2014, *Natur*, **516**, 68
- González-Alfonso, E., Fischer, J., Spoon, H. W. W., et al. 2017, *ApJ*, **836**, 11
- Gronke, M., & Oh, S. P. 2018, *MNRAS*, **480**, L111
- Gronke, M., & Oh, S. P. 2020, *MNRAS*, **492**, 1970
- Heckman, T. M., Alexandroff, R. M., Borthakur, S., Overzier, R., & Leitherer, C. 2015, *ApJ*, **809**, 147
- Hummer, D. G., & Storey, P. J. 1987, *MNRAS*, **224**, 801

- Izotov, Y. I., Chisholm, J., Worseck, G., et al. 2022, *MNRAS*, **515**, 2864-2881
- Jones, A., Kauffmann, G., D'Souza, R., et al. 2017, *A&A*, **599**, A141
- Kauffmann, G., Heckman, T. M., Tremonti, C., et al. 2003, *MNRAS*, **346**, 1055
- Kewley, L. J., & Dopita, M. A. 2002, *ApJS*, **142**, 35
- Kewley, L. J., Dopita, M. A., Sutherland, R. S., Heisler, C. A., & Trevena, J. 2001, *ApJ*, **556**, 121
- Kewley, L. J., & Ellison, S. L. 2008, *ApJ*, **681**, 1183
- Kewley, L. J., Groves, B., Kauffmann, G., & Heckman, T. 2006, *MNRAS*, **372**, 961
- Lehnert, M. D., & Heckman, T. M. 1996, *ApJ*, **462**, 651
- Leitherer, C., Schaerer, D., Goldader, J. D., et al. 1999, *ApJS*, **123**, 3
- Lochhaas, C., Thompson, T. A., Quataert, E., & Weinberg, D. H. 2018, *MNRAS*, **481**, 1873
- Lochhaas, C., Thompson, T. A., & Schneider, E. E. 2021, *MNRAS*, **504**, 3412
- Menon, S. H., Federrath, C., & Krumholz, M. R. 2022, *MNRAS*, **517**, 1313
- Molina, M., Eracleous, M., Barth, A. J., et al. 2018, *ApJ*, **864**, 90
- Moustakas, J., Kennicutt, R. C. J., & Tremonti, C. A. 2006, *ApJ*, **642**, 775
- Murray, N., Quataert, E., & Thompson, T. A. 2005, *ApJ*, **618**, 569
- Nagao, T., Murayama, T., & Taniguchi, Y. 2001, *ApJ*, **549**, 155
- Oppenheimer, B. D., Crain, R. A., Schaye, J., et al. 2016, *MNRAS*, **460**, 2157
- Peeples, M. S., Werk, J. K., Tumlinson, J., et al. 2014, *ApJ*, **786**, 54
- Perrotta, S., Coil, A. L., Rupke, D. S. N., et al. 2023, *ApJ*, in press
- Perrotta, S., George, E. R., Coil, A. L., et al. 2021, *ApJ*, **923**, 275
- Petter, G. C., Kepley, A. A., Hickox, R. C., et al. 2020, *ApJ*, **901**, 138
- Prochaska, J. X., Gawiser, E., Wolfe, A. M., Cooke, J., & Gelino, D. 2003, *ApJS*, **147**, 227
- Rich, J. A., Dopita, M. A., Kewley, L. J., & Rupke, D. S. N. 2010, *ApJ*, **721**, 505
- Rupke, D. S., Veilleux, S., & Sanders, D. B. 2005, *ApJS*, **160**, 115
- Rupke, D. S. N. 2014, IFSFIT: Spectral Fitting for Integral Field Spectrographs, Astrophysics Source Code Library, ascl:1409.005
- Rupke, D. S. N., Coil, A., Geach, J. E., et al. 2019, *Natur*, **574**, 643
- Rupke, D. S. N., Thomas, A. D., & Dopita, M. A. 2021, *MNRAS*, **503**, 4748
- Rupke, D. S. N., & Veilleux, S. 2013, *ApJ*, **768**, 75
- Rupke, D. S. N., & Veilleux, S. 2015, *ApJ*, **801**, 126
- Sanders, R. L., Shapley, A. E., Kriek, M., et al. 2016, *ApJ*, **816**, 23
- Schlafly, E. F., & Finkbeiner, D. P. 2011, *ApJ*, **737**, 103
- Schneider, E. E., Ostriker, E. C., Robertson, B. E., & Thompson, T. A. 2020, *ApJ*, **895**, 43
- Sell, P. H., Tremonti, C. A., Hickox, R. C., et al. 2014, *MNRAS*, **441**, 3417
- Sharp, R. G., & Bland-Hawthorn, J. 2010, *ApJ*, **711**, 818
- Sheinis, A. I., Bolte, M., Epps, H. W., et al. 2002, *PASP*, **114**, 851
- Shull, J. M., Smith, B. D., & Danforth, C. W. 2012, *ApJ*, **759**, 23
- Spoon, H. W. W., Marshall, J. A., Houck, J. R., et al. 2007, *ApJL*, **654**, L49
- Strickland, D. K., & Heckman, T. M. 2009, *ApJ*, **697**, 2030
- Sturm, E., González-Alfonso, E., Veilleux, S., et al. 2011, *ApJL*, **733**, L16
- Thompson, T. A., Fabian, A. C., Quataert, E., & Murray, N. 2015, *MNRAS*, **449**, 147
- Thompson, T. A., Quataert, E., & Murray, N. 2005, *ApJ*, **630**, 167
- Thompson, T. A., Quataert, E., Zhang, D., & Weinberg, D. H. 2016, *MNRAS*, **455**, 1830
- Tremonti, C. A., Moustakas, J., & Diamond-Stanic, A. M. 2007, *ApJL*, **663**, L77
- Tumlinson, J., Peeples, M. S., & Werk, J. K. 2017, *ARA&A*, **55**, 389
- Tumlinson, J., Thom, C., Werk, J. K., et al. 2011, *Sci*, **334**, 948
- Veilleux, S., Maiolino, R., Bolatto, A. D., & Aalto, S. 2020, *A&ARv*, **28**, 2
- Veilleux, S., & Osterbrock, D. E. 1987, *ApJS*, **63**, 295
- Veilleux, S., & Rupke, D. S. 2002, *ApJL*, **565**, L63
- Werk, J. K., Prochaska, J. X., Tumlinson, J., et al. 2014, *ApJ*, **792**, 8
- Whalen, K. E., Hickox, R. C., Coil, A. L., et al. 2022, *AJ*, **164**, 222
- Xu, X., Henry, A., Heckman, T., et al. 2022, *ApJ*, **933**, 202
- Zhang, D., & Davis, S. W. 2017, *ApJ*, **839**, 54